

1       **Title**

2       Paleotsunami record of the past 4300 years in the complex coastal lake system of  
3       Lake Cucao, Chiloé Island, south central Chile

4  
5       **Authors**

6       Philipp Kempf<sup>1,2</sup>, Jasper Moernaut<sup>3</sup>, Maarten Van Daele<sup>2</sup>, Mario Pino<sup>4</sup>, Roberto  
7       Urrutia<sup>5</sup>, Marc De Batist<sup>2</sup>

8  
9       **Affiliations**

- 10       1) Institute of Geological Sciences, Freie Universität Berlin, Berlin Germany  
11       2) Renard Centre of Marine Geology, Ghent University, Gent, Belgium  
12       3) Institute of Geology, University of Innsbruck, Innsbruck, Austria  
13       4) Instituto de Ciencias de la Tierra, Universidad Austral de Chile, Valdivia, Chile  
14       5) Centro EULA Chile, Universidad de Concepción, Concepción, Chile

15  
16       **Abstract**

17       In CE 1960, Lake Cucao on Chiloé Island in south central Chile, was inundated by the  
18       tsunami of the Great Chilean Earthquake ( $M_w$  9.5). The area of what is now the lake  
19       basin is submerged since the end of the rapid postglacial sea level rise and may have  
20       recorded tsunami inundations in its sedimentary record since then. Sub-bottom  
21       profiles and side scan sonar data reveal a tidal delta with a crosscutting channel,  
22       which controls the sedimentary environment in the coast-facing part of Lake Cucao.  
23       The convergent pattern of sub-bottom reflections near this channel indicates that tidal  
24       currents were active in the lake at least episodically since the formation of a major  
25       unconformity with strong reflection amplitude, i.e. the onset of lacustrine  
26       sedimentation. A radiocarbon date at the base of one of the 21 collected sediment  
27       cores dates this reflector to ~3800 yrs BP. Little net vertical displacement in  
28       combination with an outlet river channel that can act as a pathway for sediment  
29       transport appears to have maintained the sensitivity of Lake Cucao to record tsunamis  
30       in its sedimentary record. The sub-bottom profiles show a succession of antidunes, of  
31       which the geometry is used to reconstruct the flow speed and depth of the flow that  
32       formed them to  $6.8 \text{ m s}^{-1}$  and 4.8 m, respectively. The sedimentary record contains 15  
33       clastic layers which are interpreted as tsunami deposits with a varying level of  
34       confidence. The confidence level on the tsunami interpretation depends on five  
35       criteria; there are site-specific criteria, i.e. i) high magnetic susceptibility of the  
36       sediment indicating high clastic content, ii) cross core correlation indicating  
37       widespread deposition, iii) acoustic reflector correlation to the sedimentary record  
38       (also indicating widespread deposition), and general criteria, e.g. iv) presence of mud  
39       clasts, and v) age correlation to known paleotsunamis in the area. In this way 8 clastic

40 layers are interpreted as tsunami deposits with a high confidence level, 5 with a  
41 medium confidence level and 2 with a relatively low confidence level. The  
42 paleotsunami record of Lake Huelde, a mere 2 km north of Lake Cucao, contains 14  
43 or 15 tsunami deposits in the same time interval, of which at least 10 can be  
44 correlated. This study adds a long paleotsunami record on a coastline where extreme  
45 tsunamis occur frequently and where long (>2000 yrs) paleotsunami records are still  
46 sparse. This study underlines the many challenges and extraordinary advantages  
47 associated to paleotsunami research on coastal lakes and demonstrates how  
48 indispensable geophysical mapping and numerous coring sites can be in  
49 understanding the depositional environment of dynamic coastal lakes for extracting  
50 high-quality paleotsunami records.

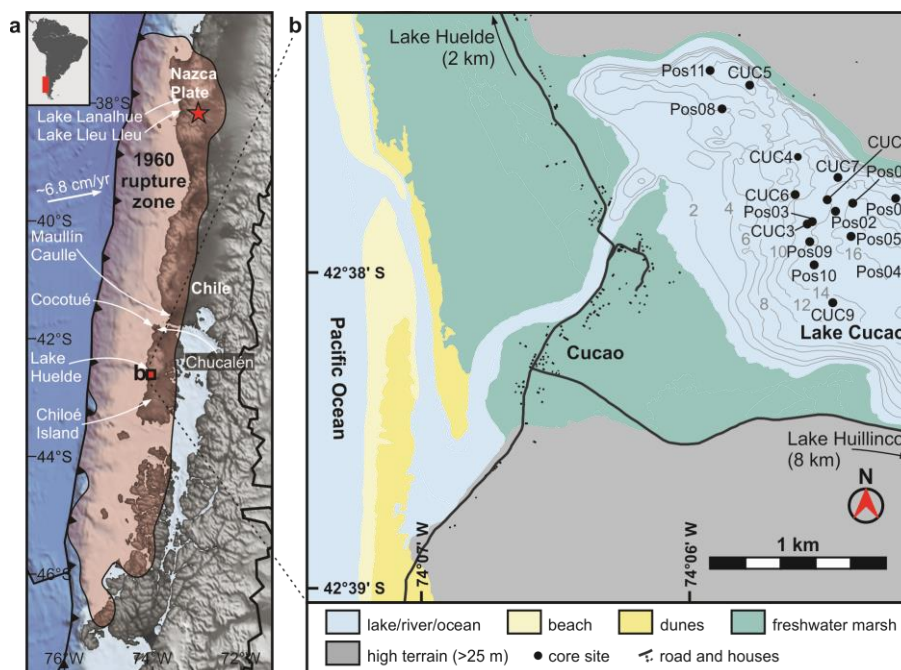
## 51 **Keywords**

52 Tsunami deposits, lacustrine sediments, sub-bottom profiles, south central Chile,  
53 coastal sediment dynamics.

## 54 **1 Introduction**

55 Long and continuous sedimentary records of infrequent large-scale tsunamis are  
56 essential in characterising recurrence patterns – a requisite for reliable hazard  
57 assessments. During the past decades the scientific means to research the sedimentary  
58 record of tsunamis have grown in quantity and quality (Chagué-Goff et al., 2017,  
59 2011). Linking tsunami deposits to tsunamis from documented history is a necessary  
60 step to calibrate tools in paleotsunami research. However, the primary reason for  
61 sedimentological investigations is to extend the historical record which is often not  
62 long enough to capture the variability in tsunami recurrence (Kempf et al., 2018). A  
63 challenging task, because long and continuous sedimentary records in often highly  
64 dynamic coastal areas are rare.

65 Written history in south central Chile begins with the Spanish invasion in CE 1541  
66 (Cisternas et al., 2005; Lomnitz, 2004, 1970). In the ~500 years since then, four major  
67 earthquakes were chronicled in the area between the Arauco peninsula (~37°S) and  
68 the Chile Triple Junction (~46°S). The latest was the CE 1960 Great Chilean  
69 Earthquake ( $M_w$  9.5), notorious for being the strongest earthquake on instrumental  
70 record. The older events occurred in CE 1575, 1737 and 1837. According to damage  
71 reports, tsunamis damaged coastal towns in all but the CE 1737 earthquake.  
72 Sedimentological investigations produced evidence for tsunami inundation for all  
73 three documented tsunamis in a multitude of coastal areas of Chile (Atwater et al.,  
74 2013; Cisternas et al., 2017, 2005; Dura et al., 2015; Ely et al., 2014; Garrett et al.,  
75 2015; Kempf et al., 2015; Nentwig et al., 2015; Reinhardt et al., 2010). In addition,  
76 six sites, i.e. Tirúa (Nentwig et al., 2018), Maullín (Cisternas et al., 2005), Caulle  
77 (Atwater et al., 2013), Chucalén (Garrett et al., 2015), Cocotué (Cisternas et al., 2017)  
78 and Lake Huelde (Kempf et al., 2017) are known to have recorded tsunami inundation  
79 before written history began (Fig. 1). Of these six sites, only the Maullín and Lake  
80 Huelde records extend the tsunami history past 1000 yrs BP, highlighting the need for  
81 adequate sites that have recorded a long sedimentary tsunami record.

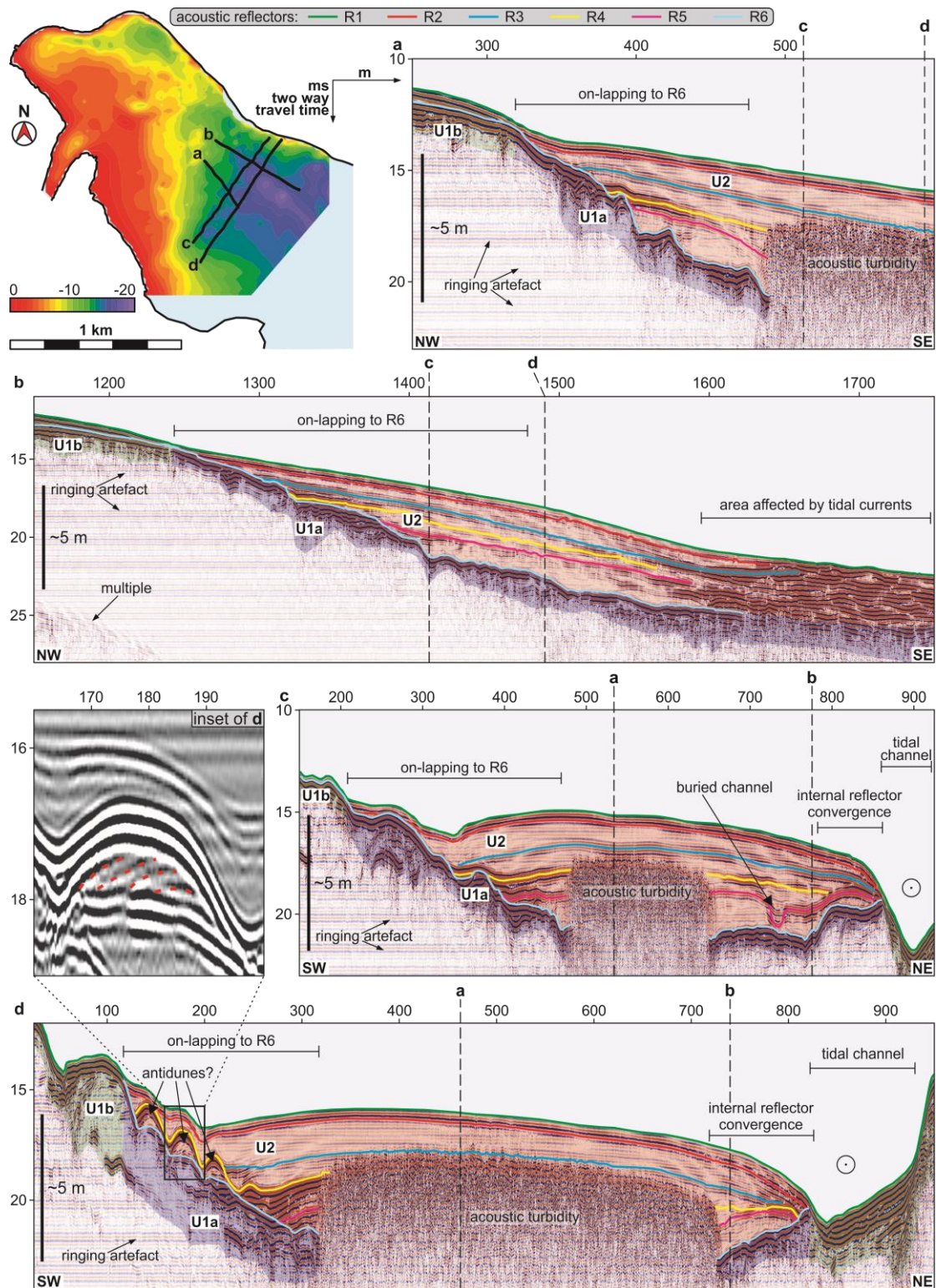


82

83 *Figure 1: a) Topographic and bathymetric overview of south central Chile. The*  
 84 *digital elevation model is based on the ETOPO1 dataset (Amante and Eakins,*  
 85 *2009). The epicentre and the 1 m slip contour line representing the rupture zone*  
 86 *(Moreno et al., 2009) of the CE 1960 earthquake are drawn in red. Locations of*  
 87 *coastal sediment records discussed in the text are indicated in white; b) detailed*  
 88 *map of the study area. The geomorphological units are based on field*  
 89 *observations and are extended using satellite imagery (Google Earth). The lake*  
 90 *bathymetry map is based on side scan sonar bottom tracks (Kempf et al., 2015).*

91 One of the difficulties when researching tsunami deposits on millennial timescales, is  
 92 relative sea level change, which plays a key role in tsunami deposition and  
 93 preservation (Dura et al., 2016; Kelsey et al., 2015). Relative sea level rise creates the  
 94 needed accommodation for tsunami deposit preservation in coastal lowlands.  
 95 However, with too much relative sea level rise or fall or coastal erosion or  
 96 progradation, the shoreline displacement may shift the area of tsunami deposition in  
 97 respect to the previous tsunami deposit, which makes long and continuous  
 98 paleotsunami records from coastal lowlands rare. In contrast, coastal lakes can  
 99 provide excess accommodation and may be in a position with a stable sensitivity to  
 100 record tsunami inundation since the culmination of the early Holocene sea level rise.

101 This study partially builds on a chapter in the doctoral thesis of the first author  
 102 (Kempf, 2016). It presents a long and continuous sedimentary record from coastal  
 103 Lake Cucao, with multiple tsunami deposits reaching back to ~4300 yrs BP based on  
 104 a dense coverage of acoustic data and 21 sediment cores. The quality of the tsunami  
 105 record is assessed by evaluating the sedimentary environment, tsunami deposit  
 106 composition and age correlation with paleotsunamis in the region. The spatial  
 107 multiproxy approach allows us to assign a confidence level to the interpretation as  
 108 tsunami deposits, allowing a better evaluation of the temporal correlation of  
 109 paleotsunamis.



110

111 *Figure 2: Sub-bottom profiles show the seismic stratigraphy of Lake Cucao with*  
 112 *seismic units U1a (blue), U1b (green) and U2 (red). Profiles a) and b) parallel*  
 113 *to the lake's long axis image the on-lapping of the internal acoustic reflectors*  
 114 *R1–R5 onto acoustic reflector R6. Profiles in cross-direction to the lake's long*  
 115 *axis c) and d) show down-lapping in the southeast and convergent internal*  
 116 *reflectors towards the tidal channel. Reflector R4 expresses three hummocks (see*  
 117 *inset), which are interpreted as antidunes.*

## 118 **2 Setting**

119 Lake Cucao (74.09°W, 42.63°S) is a coastal lake located on the west coast of Chiloé  
120 Island in south central Chile (Fig. 1a). It is connected to the Pacific Ocean by its  
121 outlet river channel, which crosses the 1.3 km wide barrier of an up to 250 m wide  
122 beach, a narrow belt of active dunes followed by ancient dunes and pastures (Fig. 1b).  
123 Lake Cucao is an elongated lake with its long axis in NW-SE direction of 7.9 km and  
124 a width of ~1.5 km. It is 10.6 km<sup>2</sup> large and up to 25 m deep. It has a small catchment  
125 to lake surface ratio of 3.1:1, because of the upstream adjacent Lake Huillinco. The  
126 only direct riverine input is a small creek from the south in the eastern part. The outlet  
127 channel of the lake facilitates water exchange between lake and ocean in both  
128 directions, because the lake level lies in the intertidal zone (Kempf et al., 2015;  
129 Villalobos et al., 2003). The daily exchange of water forms a stable saline bottom  
130 water body in Lake Cucao and Lake Huillinco (Fig. 1) (Villalobos et al., 2003). With  
131 the transport of water from the Pacific comes erosion, transport and deposition of  
132 sediment, which produced a tidal delta around the outlet channel in Lake Cucao.  
133 Active mega-ripples on the tidal delta and a crosscutting channel through the delta are  
134 the bedform expressions of relatively strong present-day tidal currents (Fig. 2 and 3)  
135 (Kempf et al., 2015).

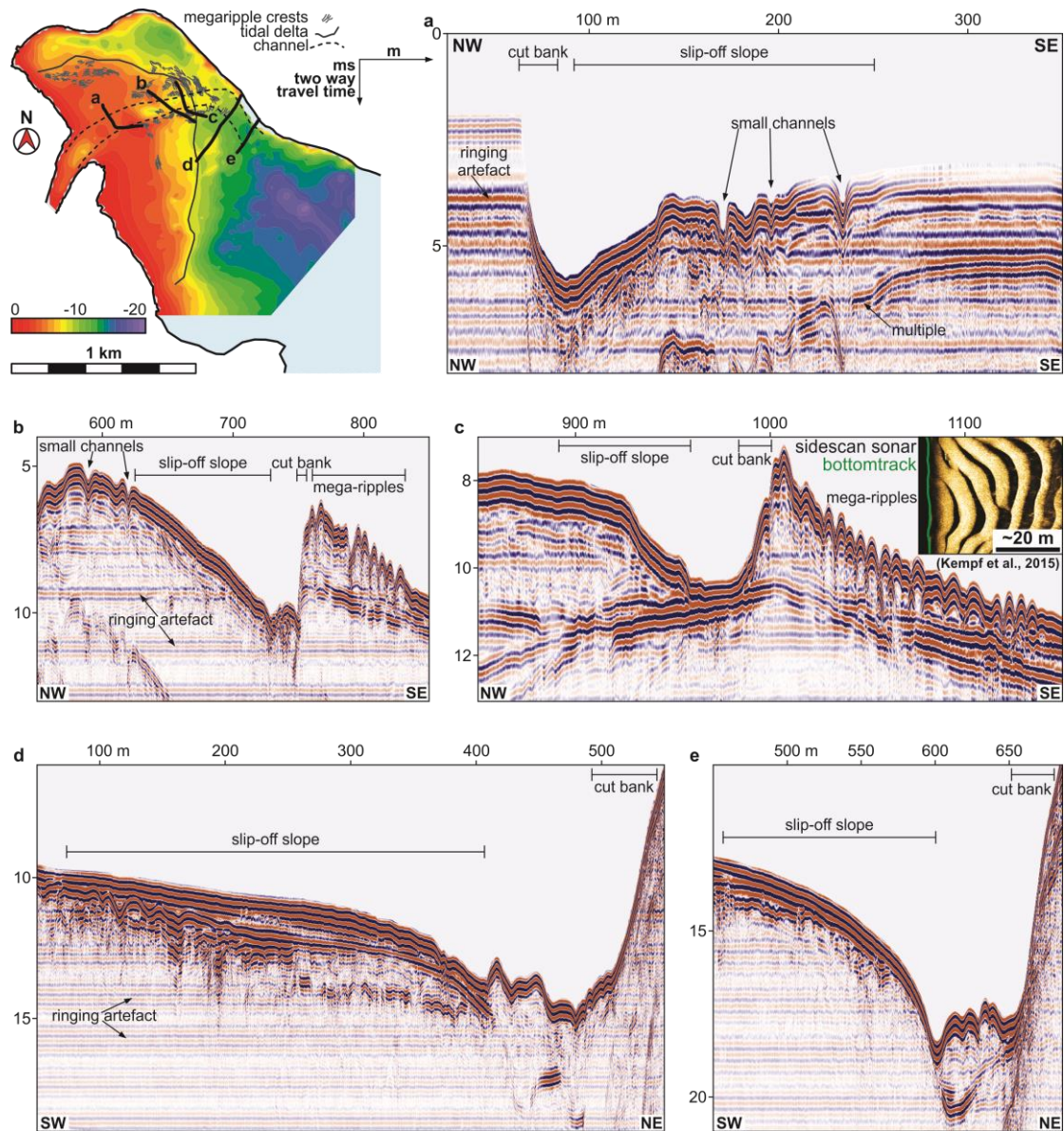
## 136 **3 Methods**

### 137 **3.1 Acoustic imaging**

138 The complex sedimentary system around Lake Cucao's outlet, was imaged with a  
139 Klein3000 side scan sonar, which uses 100 kHz and 500 kHz frequencies to produce a  
140 50 m wide swath of the lake floor's acoustic reflectivity. The data was visualised with  
141 SonarWizMap v4 and has been presented in detail in Kempf et al. (2015). Here, we  
142 make use of the mapped mega-ripple crest outlines (Fig. 3).

143 We collected 25 km of high-resolution sub-bottom profiles with a 3.5 kHz  
144 GeoAcoustics GeoPulse pinger in 71 lines. At 3.5 kHz, the vertical resolution is  
145 between 10 and 20 cm. The data was visualised and interpreted with IHS Markit  
146 Kingdom v8.8. We use the sub-bottom profiles to

- 147 i) image the sedimentary architecture of the lake basin infill,
- 148 ii) to map geomorphologic features.
- 149 iii) to describe the general seismic stratigraphy,
- 150 iv) to determine coring sites,
- 151 v) to integrate the sediments cores with the acoustic data (ground truthing)



152

153 *Figure 3: Sub-bottom profiles across the tidal channel expressing the asymmetry of*  
 154 *the channel with alternating slip-off slopes and cut banks. Tidal currents*  
 155 *produce mega-ripples outside the cut bank and small channels are present on the*  
 156 *upper bank of the slip-off slope.*

### 157 **3.1 Sediment core analysis**

158 In total, we cored at 21 locations in Lake Cucao, 9 of which were cored deeper than 2  
 159 m burial depth, with a maximum of ~8 m burial depth recovered. The top core section  
 160 at each coring site is comprised of a gravity core, because gravity corers produce  
 161 relatively undisturbed near-surface sediment samples. Any deeper core sections were  
 162 obtained with a UWITEC hammer-driven piston corer. Deep and full recovery was  
 163 achieved by overlapping 3-m-long core sections to produce composite cores. Both  
 164 types of cores have a 6 cm inner diameter.

165 Each split core was analysed with a multi-sensor core logger (Geotek MSCL) for  
 166 high-resolution line scan core surface imagery, gamma ray attenuation density

167 logging and magnetic susceptibility logging (Bartington MS2E point sensor). The  
 168 organic content was estimated using protocols in Heiri et al. (2001) for loss on  
 169 ignition to 550 °C. Some core sections were X-ray CT-scanned with a Siemens Flash  
 170 medical CT-scanner with a voxel size of  $\sim 0.15 \times \sim 0.15 \times 0.6$  mm. Grain size  
 171 distributions were measured with a Malvern Mastersizer 2000 after treatment with 2  
 172 ml of 35% hydrogen peroxide to dissolve organic content (where necessary this step  
 173 was repeated), 1 ml of 10% nitric acid to dissolve calcareous content and 300 mg  
 174 sodium hexametaphosphate to prevent grain flocculation. Material for radiocarbon  
 175 dating was extracted by either identifying macrofossils or by wet-sieving 1 cm thick  
 176 slices of sediment and picking remains of plants and periostraca in the sieve (Tab. 1).

177 The age control is based on 7 radiocarbon dates (Tab. 1) and the results of Kempf et  
 178 al. (2015), who identified the youngest clastic layer as the CE 1960 tsunami deposit  
 179 by the means of  $^{137}\text{Cs}$  and  $^{210}\text{Pb}$ -dating. The radiocarbon dates were calibrated using  
 180 the southern hemisphere calibration curve SHCal13 (Hogg et al., 2013). The samples  
 181 are comprised of leaves, small plant fragments and periostraca of (probably) *Diplodon*  
 182 *chilensis* and fragments thereof. *Diplodon chilensis* is a freshwater species  
 183 (Valdovinos and Pedreros, 2007).

184 *Table 1: Radiocarbon data for fossil leaves, plant fragments and periostraca from*  
 185 *composite core Pos04, which is used as the master core for the age-control of*  
 186 *the Lake Cucao sedimentary record.*

sample ID	core ID	section depth	core depth in event-free age model	material	lab ID	14Cage	14Cage error
		cm	cm			14C yrs BP	yrs
CUCA10B-1.5	CUCA10B	1.5	142.5	shell fragment and plant fragments	UBA-37365	26178	161
CUCA10B-51	CUCA10B	51	190	plant fragments	UBA-37369	5189	56
CUCA11A-52	CUCA11A	52	246	plant fragments	UBA37370	2360	63
CUCA11A-101.5	CUCA11A	101.5	285.5	plant and periostracum fragments	UBA-37368	2166	34
CUCA11B-22	CUCA11B	22	313	plant fragments	UBA-37367	2342	33
CUCA11B-91.5	CUCA11B	91.5	353.5	periostracum	UBA-37364	2829	38
CUCA12B-82.5	CUCA12B	82.5	504	leaf	UBA-21476	3445	34

187

## 188 4 Results

### 189 4.1 Seismic stratigraphy

190 Two seismostratigraphic units can be differentiated on sub-bottom data from Lake  
 191 Cucao, U1 and U2 (Kempf et al., 2015). U1 (a and b) includes the acoustic base of the  
 192 sedimentary infill. They laterally merge into one another. U1a is covered by the lake's  
 193 sedimentary infill in relatively deep areas, whereas U1b is at least sporadically  
 194 reworked by tidal currents entering and exiting the lake in shallow areas near a tidal  
 195 channel and not covered by lake infill (Fig. 2). U2 is the lacustrine sediment infill.  
 196 The basal contact of U2 to U1a creates an unconformity (reflector R6) characterized  
 197 by on-lapping reflector terminations towards the west. The internal reflector geometry  
 198 of U2 in the upper part (above reflector R4) is parallel to sub-parallel with a low-  
 199 amplitude acoustic facies including infrequent high amplitude, continuous reflections.

200 (Fig. 2c). The lower part of U2 (below reflector R4) describes a more complex infill  
201 pattern with few internal unconformities.

202 The presence of shallow gas in the sediment of the central basin causes acoustic  
203 turbidity, which blanks the internal reflector geometry of U2 at depths greater than  
204 ~1.5 m (2 ms two-way-travel time, TWT). In total, five parallel to sub-parallel  
205 reflectors (R1–R5) can be traced within U2. R1 represents the lake floor and produces  
206 a continuous, strong reflection with decreasing amplitude towards the deeper lake  
207 basin in the southeast (Fig. 2). R2–R5 show high-amplitude, continuous internal  
208 reflections and form on-laps to either R6 or to one of the other internal reflectors, e.g.  
209 R4 on-laps to R5 in some areas. Of all internal reflectors, R4 has the highest reflection  
210 amplitude and marks the top of a hummocky paleo-surface in the south of the  
211 surveyed area (Fig. 2d). The hummocks are ~30 m long and ~1 m thick with up-slope  
212 dipping internal reflections. The two lowermost internal reflectors, R4 and R5, exhibit  
213 erosion of the underlying acoustically transparent lake sediment in the form of few  
214 buried channels (Fig. 2c).

215 The tidal channel incises the shallow delta up to 3.5 m deep and ~100 m wide, at its  
216 western end as a prolongation of the outlet river channel (Fig. 3a). The bathymetric  
217 cross-profiles of the channel are asymmetric with a flatter slip-off slope and a steeper  
218 cut bank of the channel (Fig. 3). The asymmetry alters along the channel. About 10 m  
219 wide and 0.5 m deep incised channels are common on the upper slip-off slope. Mega-  
220 ripples with about 8 m ripple wavelength and ~0.4 m ripple height are abundant  
221 around the incised channel, with a concentric arrangement (Kempf et al., 2015). The  
222 channel continues towards the north-eastern shore (Fig. 3b, c) and bends south-  
223 eastward to align with the long axis of the lake from where it continues parallel to the  
224 north-eastern shoreline (Fig. 3d, e). Towards the channel, the parallel to sub-parallel  
225 sedimentary infill of U2 (R1–R5) becomes convergent (Fig. 2c, d).

#### 226 **4.2 Lacustrine sedimentation**

227 On the intertidal delta and in the crosscutting channel, i.e. areas where the top of U1b  
228 is at the lake floor, the sediment consists of a well-sorted medium to fine sand with  
229 mostly quartz, feldspar, hornblende and mica minerals (Fig. 4, e.g. core CUC7). The  
230 coarse and moderately to well sorted sand prevented penetration deeper than 20 cm  
231 with the coring equipment in these locations. This sand is mostly massive with some  
232 occurrences of 1 cm thick grey muddy layers. The magnetic susceptibility of this sand  
233 is very high, sometimes exceeding  $1000 \times 10^{-5}$  SI.

234 Sediment from the lake basin consists mostly of brown to black homogenous, poorly  
235 sorted organic-rich mud. The transition from black to brown mud can be gradual or  
236 sharp. In the case of sharp transitions, the brown mud is on top. The organic content  
237 for both black and brown mud is between 20 and 35 % and consists of seeds, fibrous  
238 plant material, pollen and fragments of bivalve periostraca without the calcareous  
239 shell. The periostraca are sometimes fully preserved with distinct growth rings and are  
240 probably from *Diplodon chilensis*, the most common freshwater clam in southern and



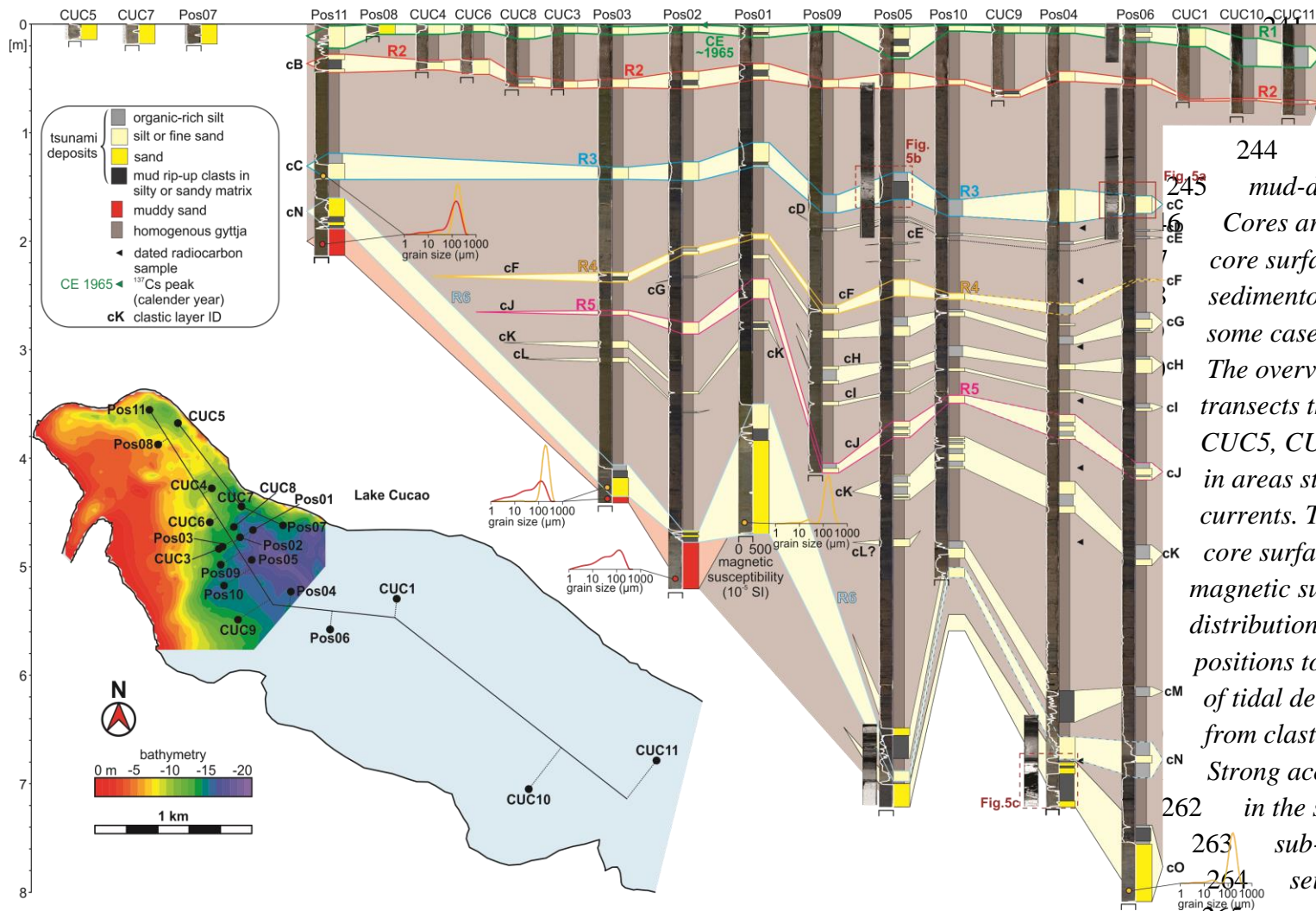
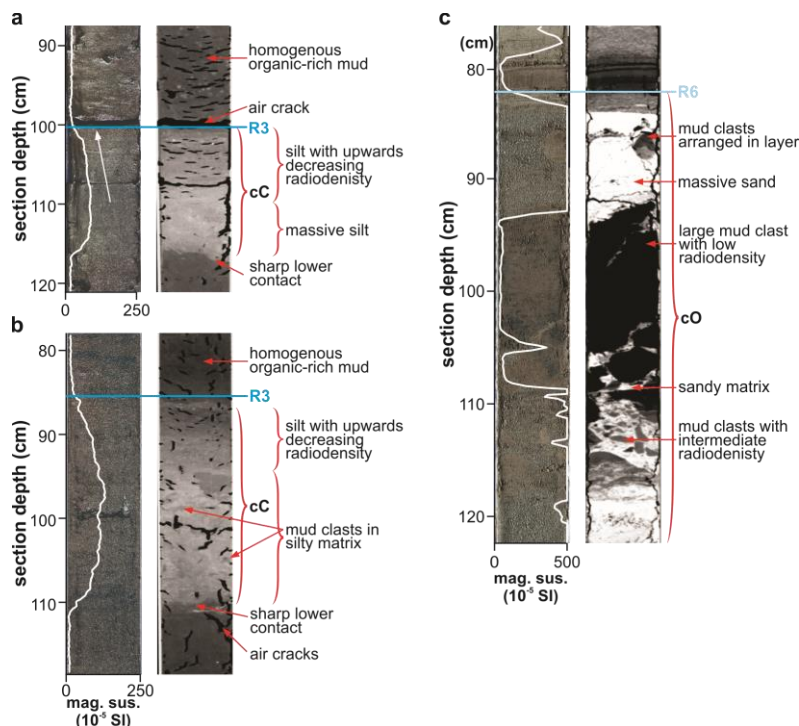


Figure 4: Core to core correlation of clastic 244 layers in the organic-rich mud-dominated lake sediments. Cores are represented by a split core surface image, a sedimentological core log and in some cases 2D slices of CT-scans. The overview map shows two core transects through the lake. Cores CUC5, CUC7 and Pos07 are located in areas strongly affected by tidal currents. The white line on the split core surface images represents magnetic susceptibility. Grain size distributions are shown in 7 different positions to differentiate muddy sand of tidal delta foresets (red lines) from clastic layers (orange lines). Strong acoustic reflectors are drawn in the same colour as they are on sub-bottom profiles. The seismic to core correlation is captured in figure 6.

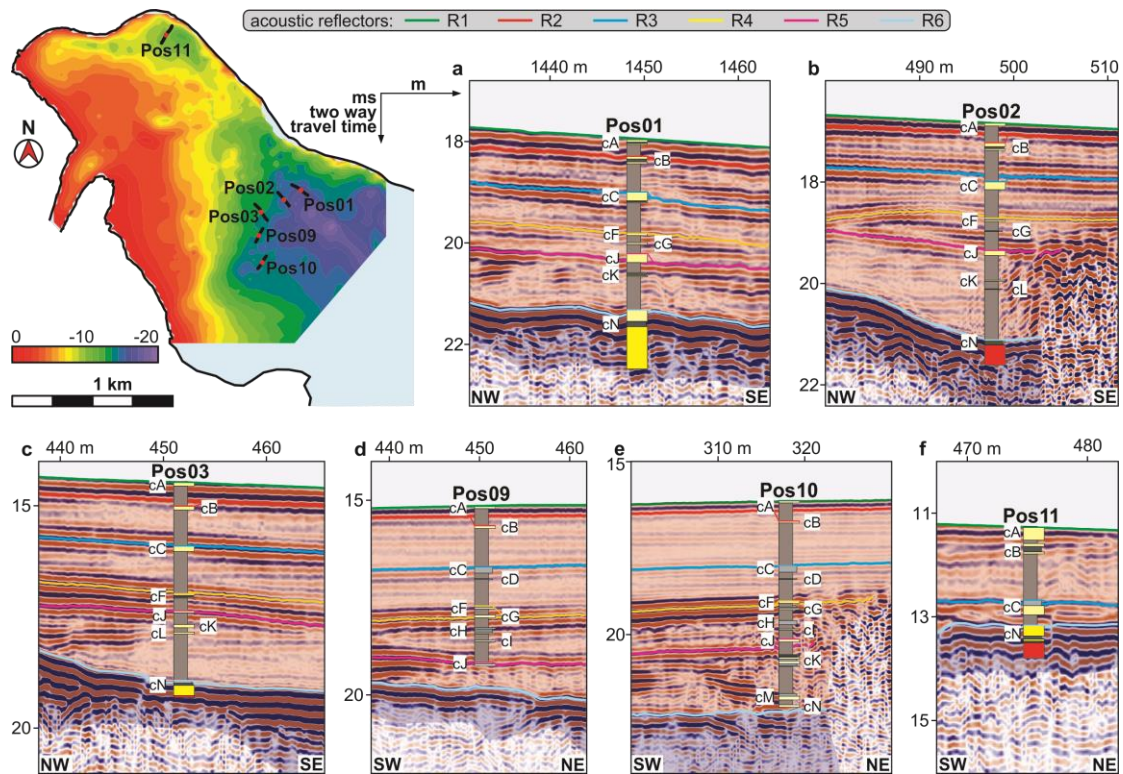


266

267 *Figure 5: X-ray CT-scans of selected core sections. Lighter grey means higher*  
 268 *radiodensity. a) and b) CT-scans of clastic layer cC associated acoustic reflector*  
 269 *R3; c) clastic layer cN under acoustic reflector R6. All clastic layers exhibit a*  
 270 *sharp contact at the bottom. CT-scans in a) and b) show upwards decreasing*  
 271 *radiodensity. In b) and c) mud clasts with two differing CT-densities are*  
 272 *surrounded by silty (b) to sandy (c) matrix.*

273 south central Chile. The organic-rich mud smells strongly of hydrogen sulphide when  
 274 cores are opened the first time (both during fieldwork and in the lab), indicating  
 275 hypoxic or anoxic conditions. The magnetic susceptibility is low between 0 and  $40 \times$   
 276  $10^{-5}$  SI (Fig. 4 and 5).

277 In all 9 long cores, there are 1 to 30 cm thick layers with high clastic content. The  
 278 medium silt to fine sand of the clastic layers is coarser than the clastic fraction of the  
 279 organic-rich mud below and above. However, the clastic layers always contain a  
 280 fraction of organic matter, too. The magnetic susceptibility signal of these layers  
 281 ranges from relatively low, with values between  $40$  and  $100 \times 10^{-5}$  SI, to relatively  
 282 high, with values up to  $500 \times 10^{-5}$  SI and higher (Fig. 4 and 5). The clastic layers are  
 283 often visually indistinguishable from the organic-rich mud on the split core surface,  
 284 except for black to brown colour contrasts. CT-scans of the clastic layers reveal sharp  
 285 lower contacts with the highest radiodensity at the base, gradually decreasing upwards  
 286 (Fig. 5a, b). Some clastic layers bear 1 to 3 cm large mud clasts in a matrix of sand or  
 287 silt. The mud clasts have lower radiodensity than the matrix and are discernible on  
 288 CT-scan as darker bodies (Fig. 5b). The mud clasts were difficult to impossible to  
 289 identify on split core surfaces except for clastic layer cN. All other mud clasts were  
 290 identified on X-ray CT-scans. If the clastic layers are brown, then they often coincide  
 291 with a sharp colour transition from black to brown at their base. Some clastic layers  
 292 have recognisable characteristics, e.g. thickness, colour, shape of the magnetic



293

294 *Figure 6: Seismic to core correlation of the CE 1960 tsunami deposit (cA) and clastic*  
 295 *layers cB to cN (cO not represented on this figure) with strong acoustic*  
 296 *reflectors R1 to R6. The assumption of uniform p-wave velocity within the entire*  
 297 *lake infill and the piston coring process can cause minor offsets between cores*  
 298 *and acoustic reflectors on sub-bottom profiles.*

299 susceptibility log etc. that can be traced laterally throughout the basin. This way the  
 300 easiest-to-trace clastic layers were correlated, helping with the correlation of the other  
 301 clastic layers.

302 The clastic layers are labelled from cA to cO, where “c” stands for Lake Cucao and  
 303 the capital letter is in alphabetical order down core. This is in analogy to the Lake  
 304 Huelde record 2 km north of Lake Cucao, where similar layers interpreted as tsunami  
 305 deposits, are labelled hC, hD, and so on to hQ (Kempf et al., 2017). The topmost  
 306 clastic layer in Lake Cucao was identified in Kempf et al. (Kempf et al., 2015) as the  
 307 tsunami deposit of the CE 1960 tsunami and will be called CE 1960, instead of cA.

308 Seven of 9 long cores contain the clastic layer cN in the lowest part of the  
 309 sedimentary record, which is markedly coarser (fine to medium sand) and exhibits  
 310 higher magnetic susceptibility values than the other clastic layers, with peaks up to  
 311  $2500 \times 10^{-5}$  SI. Like in all other clastic layers, the sand of cN does not contain mica.  
 312 The lack of mica distinguishes the sand of the clastic layers from the sand in samples  
 313 from the tidal delta and the crosscutting channel (Kempf et al., 2015). In cN, intervals  
 314 of well-sorted massive sands are intercalated with intervals of mud clasts in a sandy  
 315 matrix. The mud clasts can exceed the size of the core liner (6 cm) and are up to 11  
 316 cm thick. Smaller mud clasts are often arranged along horizons (Fig. 5c). Based on  
 317 the radiodensity of the mud clasts, two types can be differentiated; one type with a

318 *Table 2: Summary of confidence levels for the interpretation of tsunami deposits for*  
 319 *each clastic layer in Lake Cucao, with age and age-correlation to a known*  
 320 *tsunami, maximum magnetic susceptibility, traceability of the clastic layers*  
 321 *throughout the sedimentary record, correlation to acoustic reflections and*  
 322 *content of mud rip-up clasts.*

event name	median age (95% age interval)	potential age- correlation to published tsunami deposits	max. magnetic susceptibility	traceability in the sedimentary record	correlated to acoustic reflector	mud rip-up clasts	confidence level
	yrs BP		(10 <sup>-5</sup> SI)	represented in cores/cores reaching this depth interval			
cA/CE 1960	-7 (-11 to -5)	yes	677	18/18	R1	yes	high
cB	287 (185 - 418)	yes	695	17/17	R2	yes	high
cC	1081 (894 - 1274)	maybe	1601	9/9	R3	yes	high
cD	1226 (1031 - 1418)	yes	57	5/8	-	not observed	medium
cE	1274 (1079 - 1466)	maybe	51	2/8	-	not observed	low
cF	1656 (1454 - 1656)	yes	581	8/8	R4	yes	high
cG	1825 (1624 - 1986)	yes	431	7/8	-	not observed	medium
cH	1962 (1765 - 2109)	yes	202	5/8	-	not observed	medium
cI	2099 (1914 - 2213)	no	335	5/8	-	not observed	medium
cJ	2254 (2077 - 2322)	yes	306	8/8	R5	yes	high
cK	2530 (2378 - 2662)	yes	377	7/7	-	yes	high
cL	2883 (2670 - 3001)	no	92	3/7	-	not observed	low
cM	3699 (3530 - 3906)	yes	585	4/4	-	yes	high
cN	3783 (3612 - 3994)	yes	2269	8/8	R6	yes	high
cO (in model)	3798 (3626 - 4011)	no	1656	3/3	-	not observed	medium
cO (corrected)	4101 (3959 - 4344)	"	"	"	"	"	"

323

324 low radiodensity (black) and one type with an intermediate radiodensity (dark grey)  
 325 (Fig. 5c). The sand of the matrix and intervals of massive sand contain grains of  
 326 orthoclase, plagioclase, quartz, iron oxides (responsible for the high magnetic  
 327 susceptibility), hornblende and rarely zircon, as well as lithic grains. The same  
 328 composition of sand is reported for the CE 1960 deposit in Lake Cucao and Lake  
 329 Huelde and for the beach sand and dunes sand between Lake Cucao and the Pacific  
 330 Ocean (Kempf et al., 2015).

331 Three cores (Pos02, Pos03 and Pos11) contain poorly sorted, muddy sand at their base  
 332 (Fig. 4). The muddy content makes this sand distinctly different in grain size from the  
 333 well-sorted sand in the coarser clastic layers, e.g. clastic layers cC and cN. It consists  
 334 of the same minerals and lithic grains as the sand on the tidal delta and in the channel.

### 335 **4.3 Sub-bottom profiles to core correlation**

336 Six of the long cores were projected on sub-bottom profiles that show acoustic  
 337 penetration of the entire seismic unit U2 (Fig. 6). The correlation between cores and  
 338 the sub-bottom profiles is performed under the assumption of a constant p-wave  
 339 velocity in the entire sedimentary sequence and no vertical deformation during  
 340 hammer-driven piston coring and then tying key marker layer with the sub-bottom  
 341 profile. Realistically, variability in p-wave velocity is expected to produce minor  
 342 offsets. The vertical deformation during hammer coring will cause net compression  
 343 and wave action on the lake while coring can cause extension, which will likely be

344 heterogenous and may produce significantly larger offsets. Some offsets are indicated  
345 on the sub-bottom profiles to core correlation (Fig. 6).

346 The six reflectors of U2 (R1 to R6) can all be confidently correlated to clastic layers  
347 in the cores (Fig. 4). The top of the CE 1960 tsunami deposit is buried by  $\leq 3$  cm of  
348 lacustrine sediment in the western part of Lake Cucao (Kempf et al., 2015), which is  
349 below the vertical resolution of the sub-bottom profiles (vertical resolution between  
350 10 and 20 cm). R1, the uppermost strong reflector therefore correlates to the lake  
351 floor as well as the top of the CE 1960 tsunami deposit. R2 correlates to clastic layer  
352 cB. However, R2 is so close to the lake floor and R1 reflection, that interference of  
353 reflections may lead to a poor identification of R2 in most cases. R3 correlates to cC,  
354 R4 to cF and R5 to cJ, which are major traceable clastic layers in the sedimentary  
355 record of Lake Cucao. They tend to be especially thick and coarse, and are  
356 represented in most or all cores containing that specific stratigraphic interval. R6 is  
357 the reflector that sticks out, because reflectors R2 to R5 on-lap to it. Even though a  
358 spatial feature such as on-lapping is difficult to observe by comparison of multiple  
359 cores, clastic layers cF to cM appear to on-lap to cN (Fig. 4). Because of its  
360 stratigraphic position, the on-lapping and the strong sedimentary contrast between  
361 organic-rich mud and the medium sand of clastic layer cN, we correlate the high-  
362 amplitude reflector R6 to the coarse clastic layer cN (Tab. 2).

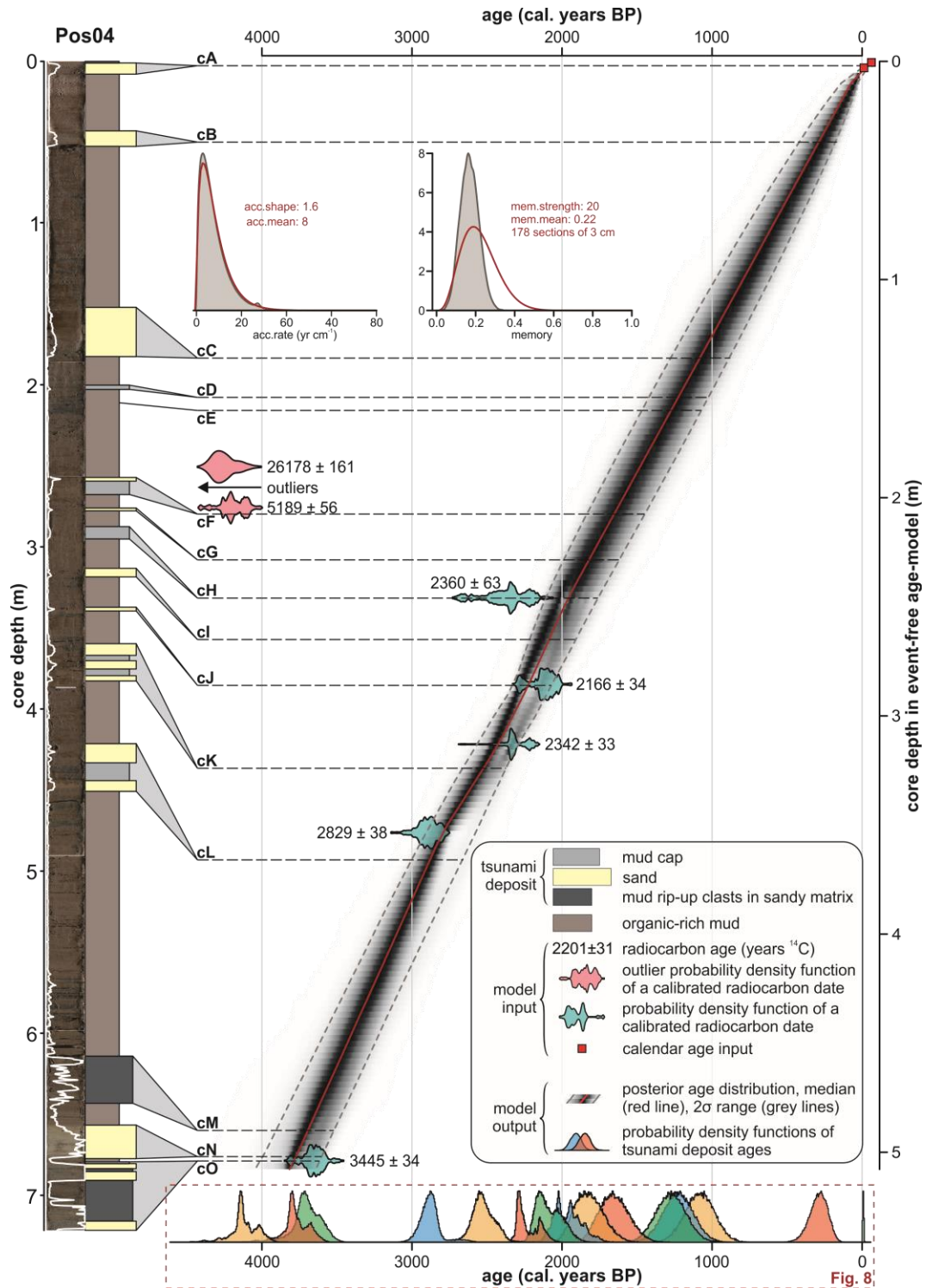
#### 363 *4.4 Age control*

364 The clastic layers exhibit characteristics of abrupt deposition, e.g. sharp lower  
365 contacts, mud clasts and decreasing upwards radiodensity, which often reflects fining  
366 upwards (cf. Van Daele et al., 2014). The intervals of the clastic layers are therefore  
367 likely to have been deposited with a different accumulation rate from the rest of the  
368 sedimentary record, most likely quasi-instantaneously.

369 We used composite core Pos04 to develop an age-depth model for Lake Cucao. The  
370 prior age-depth information consists of the following data and considerations:

- 371 i) radionuclide data that identified the CE 1960 tsunami deposit (Kempf et  
372 al., 2015)
- 373 ii) 7 radiocarbon dates (Tab. 1)
- 374 iii) clastic layers were treated as instantaneous deposits, i.e. they were taken  
375 out of the core for age-depth modelling
- 376 iv) the sediment is a lacustrine sedimentary sequence, so we assume a  
377 relatively stable sedimentation. This is supported by the uniform nature of  
378 the sediment sequence with parallel reflections on sub-bottom profiles at  
379 the core site.

380 All age-depth information of Pos04 was fed into the autoregressive Bayesian age-  
381 depth modelling algorithm BACON (Blaauw and Christen, 2011). The parameters  
382 were adjusted to divide the core into 178 sections of 3 cm and to reflect the relatively  
383 stable lake environment, i.e. continuous sedimentation of the organic-rich lacustrine  
384 mud (Fig.7).



385

386 Figure 7: Bayesian age-depth model of core Pos04 in Lake Cucao calculated with  
 387 BACON (Blaauw and Christen, 2011). The core surface image and  
 388 sedimentological core log are displayed on the left. The tsunami deposits  
 389 are treated as instantaneous deposits and are taken out of the core for age-depth  
 390 modelling. The bottom x-axis shows the model results for all tsunami deposits as  
 391 coloured age distributions.

392 The model output shows that there are two obvious outliers, i.e. extreme age  
 393 reversals, among the radiocarbon dates (samples CUCA10B-1.5 and CUCA10B-51),

394 which were neglected by the age-depth algorithm for making the age-depth model.  
395 From the resulting age-depth model we extracted the age probability distributions of  
396 all clastic layers that were treated as instantaneous deposits (Fig. 7). The problem  
397 connected to the relatively long interval of interpolation between the core top and the  
398 shallowest radiocarbon date ( $2360 \pm 63$  yrs BP) is minimised by the relatively stable  
399 sedimentary environment at core site Pos04.

400 The assumption of relatively stable accumulation rates in Pos04 (iv) appears to fail  
401 only at the lowest end of the sedimentary record (between clastic layers cN and cO).  
402 This becomes evident when comparing the 2 cm thick organic-rich mud interval in  
403 core Pos04 with the 43.5 cm thick organic-rich mud interval of the same stratigraphic  
404 position in core Pos06. The age-depth model on core Pos04 likely underestimates the  
405 time difference between clastic layers cN and cO. Using the average accumulation  
406 rate of the entire record down to clastic layer cN of  $\sim 1.31$  mm yr<sup>-1</sup> (502 cm of  
407 sediment accumulation in 3845 years), clastic layer cO is probably  $\sim 330$  years older  
408 than clastic layer cN.

## 409 5 Discussion

### 410 5.1 Antidunes as a product of tsunami inundation in Lake Cucao

411 The hummocks with the up-slope dipping internal reflectors underneath R4 (clastic  
412 layer cF) are interpreted as antidunes due to their height and length in combination  
413 with the up-slope dipping internal reflectors. Antidunes form in the upper stage  
414 supercritical flow regime. The wavelength of antidunes is related to the wavelength of  
415 the standing wave that produced them (Allen, 1984), which in turn is proportional to  
416 the square of the flow speed during formation (Kennedy, 1963). The resulting  
417 relationship between flow speed and wavelength of the antidune bedform is described  
418 by Carling (2009) with

$$419 \quad U = \sqrt{\frac{g L_a}{2\pi}} \quad (1)$$

420 Where  $U$  is the flow speed,  $g$  the gravitational acceleration on earth and  $L_a$  the  
421 average wavelength in a train of antidune bedforms. The flow depth  $d$  in dependence  
422 on average wavelength is expressed by

$$423 \quad d = \frac{L_a}{2\pi} \quad (2)$$

424 According to equation (1) the flow speed during antidune formation was  $\sim 6.8$  m s<sup>-1</sup>  
425 ( $24.6$  km h<sup>-1</sup>) and according to equation (2) the flow depth was  $\sim 4.8$  m. Both  
426 dimensions compare well with directly measured flow properties of recent large-scale  
427 tsunami inundations (cf. Fritz et al., 2012). The location of the antidunes suggests that  
428 the freshwater marsh, which now accommodates most inhabitants of the village of  
429 Cucao was washed over by strong, certainly destructive water currents. Despite their  
430 size, antidunes form relatively quickly once supercritical flow develops. However,  
431 with three antidunes of similar shape and size, we argue that supercritical flow was  
432 well developed, steady and sustained.

433 *5.2 Age control and accumulation rate variability in Lake Cucao*

434 There is no overall strong spatial variability in accumulation rate between long cores  
435 from the western part of the basin, which is indicated by sub-parallel clastic layers in  
436 the core to core correlation. This is confirmed by parallel to sub-parallel reflectors R1  
437 to R5 on sub-bottom profiles (Fig. 2a, b).

438 There are three exceptions, which are

- 439 i) confined areas of erosional truncation in form of small channels (Fig. 2c),
- 440 ii) the area close to the crosscutting channel along the north-eastern side of  
441 the lake, where the sedimentary infill becomes significantly thinner or is  
442 non-existent (Fig. 2c, d), and
- 443 iii) the deepest part of most long cores, where the strata form on-laps (this  
444 includes the age-depth modelled core Pos04 between cN and cO).

445 All long core sites avoid the areas of i) and ii).

446 In short cores CUC10 and CUC11, located 2–3 km southeast of most other cores (Fig.  
447 4), and where tidal currents are probably weaker or absent, up to 21 cm of organic-  
448 rich mud accumulated above the CE 1960 tsunami deposit. This thickness is  
449 comparable to 20–30 cm of post-1960 sediment accumulation in Lake Huelde (Kempf  
450 et al., 2015), which is currently unaffected by tidal currents. In all other cores further  
451 west in Lake Cucao the same interval is either  $\leq 4$  cm thick or missing, showing non-  
452 deposition or episodes of erosion in the post-1960 lake environment in the ocean-  
453 proximal area of the lake.

454 The age-control of the last 2000 yrs relies strongly on the assumption of stable  
455 accumulation rates between the CE 1960 tsunami deposit and the uppermost useful  
456 radiocarbon date at 246 cm (event-free core depth) (Fig. 7, Tab. 1). Cores and sub-  
457 bottom profiles justify this interpolation, because of the uniform stratigraphy with  
458 little lateral variability in this part of the stratigraphic record of U2 near the coring site  
459 Pos04.

460 Chronologies of other regional paleotsunami and paleoseismic records from south  
461 central Chile are based on similar primary age-depth information, i.e. on radiocarbon  
462 dates of plants flattened by the tsunami, rootlets in soil, terrestrial plant fragments  
463 from the pre- and post-tsunami lacustrine sediment and tephra (Atwater et al., 2013;  
464 Cisternas et al., 2017, 2005; Garrett et al., 2015; Kempf et al., 2017; Moernaut et al.,  
465 2018, 2014). The uncertainty intervals of tsunami ages in the Lake Cucao record are  
466 greater than the uncertainty intervals of the tsunami ages of, for example, the  
467 paleotsunami record of Lake Huelde. Nevertheless, the Lake Cucao ages correlate  
468 well with regional paleotsunami records (Fig. 8). The age-control can be considered  
469 of comparable quality.

470



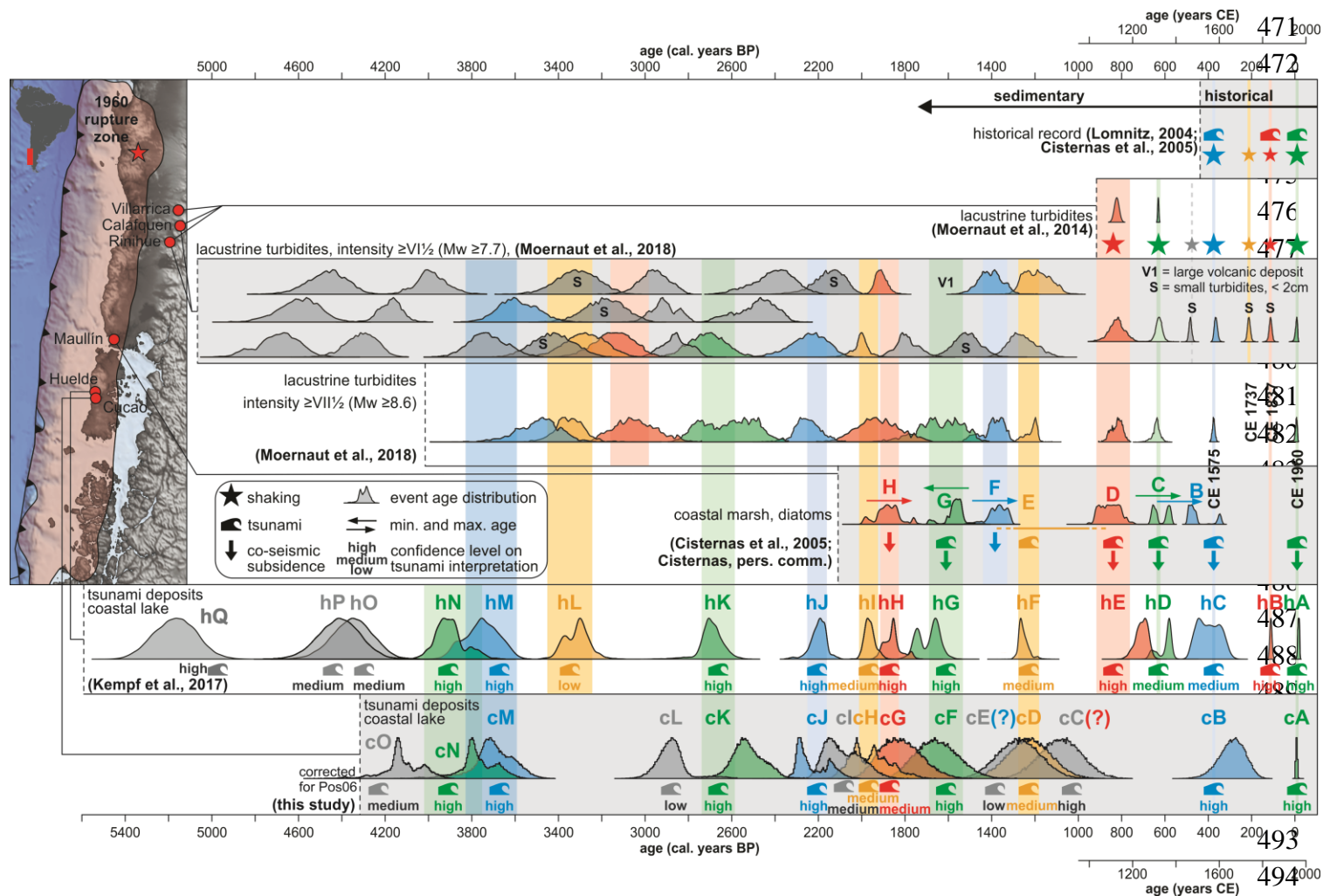


Figure 8: Regional correlation of paleoseismic and paleotsunami records. The instrumental record only includes the CE 1960 event and is not especially listed here. Documented history reveals three more large events in CE1575, 1737, 1837 (Cisternas et al., 2005; Lomnitz, 2004). Lacustrine turbidites from the Chilean lake district give paleoseismic evidence (Moernaut et al., 2018, 2014). The paleotsunami records from Maullín (Cisternas et al., 2005) and Lake Huelde (Kempf et al., 2017) offer the direct comparisons between

495 tsunami deposits. The age of cO is here corrected by 330 yrs because of the regular organic-rich lacustrine sediment between cN and cO in core  
 496 Pos06 (in contrast to core Pos04 for which the age-depth model was made).

497 ***5.3 Age of the crosscutting channel and constraints on Lake Cucao's vertical***  
498 ***displacement history***

499 Coastal areas on subduction zones are known to be prone to vertical deformation  
500 throughout the seismic cycle (Wesson et al., 2015). The CE 1960 Great Chilean  
501 Earthquake caused the area around Lake Cucao to subside co-seismically by ~1 m  
502 (Plafker and Savage, 1970), which put Lake Cucao into an intertidal position, if the  
503 lake level was not already in the intertidal zone before. The subsidence of ~1 m may  
504 have intensified the tidal currents, which would explain the limited post-CE 1960  
505 sedimentation in all but the most distal coring sites. The tidal currents entering the  
506 lake during high tide are continuing to form the intertidal delta, the crosscutting  
507 channel and the mega-ripples. Given that the sedimentary record below the CE 1960  
508 tsunami deposit appears to have stable accumulation rates, we argue that the vertical  
509 position of the river channel in relation to the relative sea level is probably at an  
510 extreme low at present in respect to the last 4300 yrs.

511 If the channel would be a recently formed feature, it would truncate the mostly  
512 parallel to sub-parallel internal reflectors of seismic unit U2. This is not the case; all  
513 internal reflectors, R1 to R5, in U2 converge towards the channel (Fig. 2c), which  
514 indicates that intertidal currents were active at least episodically during the period  
515 represented by the sedimentary infill visible on sub-bottom profiles. This constrains  
516 the net vertical displacement of Lake Cucao in the last 4300 yrs to a narrow window  
517 around its current position.

518 Additionally, river channels play a primary role in connecting the ocean with coastal  
519 lakes during tsunami inundation (Kempf et al., 2017, 2015). Consequently, regardless  
520 of the exact position of the coastline and river channel migrations, Lake Cucao may  
521 have been a reliable tsunami recorder with relatively stable sensitivity to tsunami  
522 inundation in the past 4300 yrs and potentially longer.

523 ***5.4 Identifying tsunami deposits in the Lake Cucao sedimentary record***

524 The clastic layers share similar sedimentary characteristics to the tsunami deposit of  
525 CE 1960. However, other causative processes must be excluded before a tsunami  
526 origin can be assigned. Tsunami deposits have several sedimentary characteristics,  
527 most are site-specific, and few are unique to tsunami deposits. For example,  
528 landwards thinning and landward fining sand sheets can be produced by storm surges  
529 and tsunamis alike (Kortekaas and Dawson, 2007). However, the relatively distant  
530 inland location (~1.3 km between ocean and lake) makes storm deposition in Lake  
531 Cucao unlikely. While storms occur on the south central Chilean coast, the tropical  
532 cyclones with the potential to create deposits kilometres inland and in coastal lakes,  
533 have not been documented and are unlikely to happen, even under strong El Niño  
534 conditions (Fedorov et al., 2010).

535 Excluding competing hypotheses for the formation of similar layers is equally  
536 valuable. For Lake Cucao we can, for example, exclude flood turbidites, which are  
537 not uncommon in Chilean lakes (e.g. Van Daele et al., 2019), because upstream

538 adjacent Lake Huillinco traps riverine flood input to Lake Cucao, which reduces the  
539 direct riverine input to Lake Cucao to a small creek that enters Lake Cucao from the  
540 south in its eastern part. The small creek does not have a large enough catchment to  
541 produce lake-wide flood turbidites. And if it were to produce flood turbidites the  
542 fining of sediment would be away from the inflow of the creek, i.e. east to west in the  
543 study area and not west to east.

544 We define the following five criteria for the sedimentary environment of Lake Cucao,  
545 which are either indicative of tsunami deposition or can be used to exclude other  
546 processes.

- 547 i) *High magnetic susceptibility* – Magnetic susceptibility is controlled by the  
548 ferrimagnetic mineral content of the sediment. High magnetic susceptibility in  
549 Lake Cucao means the sediment contains iron oxides (i.e. hematite and  
550 magnetite). The concentrations of ferrimagnetic minerals in the basin of Lake  
551 Cucao can be increased by organic matter depletion, compaction or by  
552 deposition of iron oxides. The low magnetic susceptibility values of organic-  
553 rich mud and the sometimes extremely high values of magnetic susceptibility  
554 in the clastic layers suggest that the layers with high magnetic susceptibility  
555 values are from extra-lacustrine sources. Processes that could provide such a  
556 sediment source are limited to lake-inundating events, such as storms and  
557 tsunamis. This effect has been described for the CE 1960 tsunami deposit  
558 ([Kempf et al., 2015](#)).
- 559 ii) *Traceability in the sedimentary record* – Tsunami deposits in coastal lakes are  
560 spatially variable in thickness ([Kelsey et al., 2005](#); [Kempf et al., 2017](#)).  
561 However, tsunami deposits are often continuous deposits to where they wedge  
562 out towards their maximum lateral extent. When tsunamis inundate coastal  
563 lakes, the water flow contains and deposits sand, remobilises muddy lake  
564 sediment and redistributes it within the lake basin. Areas beyond the zone of  
565 sandy deposition can receive exclusively muddy tsunami sediment ([Kelsey et al., 2005](#); [Kempf et al., 2017, 2015](#)). Therefore, tsunami deposits should be  
566 traceable in the sedimentary record throughout large areas of the lake, if not  
567 the entire lake basin. The criterion is given as a fraction of the number of  
568 cores, in which the clastic layer is observed over the number of cores, in  
569 which the stratigraphic interval of the clastic layer in question was recovered.  
570 Complete or nearly complete representation in the sedimentary archive is  
571 treated as indicative for tsunami deposition ([Fig. 4](#)).
- 572 iii) *Acoustic reflector correlation* – The six strong reflectors (R1–R6) on the sub-  
573 bottom profiles represent strong contrasts in acoustic impedance, i.e.  
574 differences in p-wave velocity and/or density. In an organic-rich mud-  
575 dominated environment high acoustic impedance contrast can be associated  
576 with clastic layers. Not every clastic layer will necessarily produce a high-  
577 amplitude reflector, but if a clastic layer can be correlated to a basin-wide  
578 high-amplitude reflector, then this points towards basin wide  
579

580 distribution and high clastic content, which is expected from a tsunami  
581 deposit.

582 iv) *Mud rip-up clasts* – We interpret the mud clasts as mud rip-up clasts. Mud rip-  
583 up clasts are generated by high-energy processes in otherwise low-energy  
584 environments. In sub-aquatic landslides, mud rip-up clasts occur on the  
585 spectrum of disintegration of the sliding sediment from slumps, to debris  
586 flows, to turbidity currents (cf. Lee et al., 2013). Onshore landslides that  
587 impact muddy fjord sediment have also produced mud rip-up clasts, which  
588 may show paleo flow direction by imbrication (Van Daele et al., 2014). In  
589 fluvial systems mud rip-up clasts are associated with cut bank collapses of  
590 muddy soils. In coastal environments, like marshes, mud rip-up clasts are  
591 commonly associated with tsunami deposition (Peters et al., 2007), however,  
592 storm surges reportedly can produce mud rip-up clasts, too (Phantuwongraj et  
593 al., 2013). In Lake Cucao, two types of mud rip-up clasts can be differentiated  
594 by their radiodensity. One type has the same radiodensity as the lacustrine  
595 organic-rich mud and is interpreted as such. The other type has higher  
596 radiodensity and could represent soil from the lake-surrounding marshes.  
597 Similar variations in mud rip-up clasts were described in trenches on the  
598 Chilean main land near Maullín (Atwater et al., 2013). Specifically for Lake  
599 Cucao, the presence of both types of mud rip-up clasts excludes strong tidal  
600 currents and slope failure turbidites. Tidal currents could work similarly to  
601 fluvial systems with regard to the erosional process for the source material of  
602 mud rip-up clasts and to the depositional process of clastic layers.

603 v) *Age-correlation* – Megathrust earthquake-induced tsunamis hit long stretches  
604 of coastline. Tsunami deposits can be correlated over long distances using  
605 their chronology (Cisternas et al., 2017; Peters et al., 2007). If a clastic layer  
606 correlates in age to an identified tsunami deposit elsewhere in south central  
607 Chile, then this corroborates the interpretation as a tsunami deposit. In the  
608 Lake Cucao sedimentary record, the interpretation of the CE 1960 tsunami  
609 deposit was partially based on such an age correlation. Downcore, age-  
610 correlation with the Lake Huelde sedimentary record (Kempf et al., 2017) is  
611 especially interesting, because of the lakes' proximity (2 km) to each other and  
612 the similarity of the paleotsunami record, despite the difference in lacustrine  
613 sedimentary environments.

614 Two of the 15 clastic layers (cE, and cL) fulfil only one or no criterion at all. The  
615 confidence of an interpretation as a tsunami deposit in these cases is low, however, a  
616 tsunami origin is probably still the most favourable hypothesis (Tab. 2). Eight clastic  
617 layers fulfil three or more criteria and the confidence level for interpreting these  
618 layers as tsunami deposits is high. The remaining 5 clastic layers fulfil two criteria  
619 sufficiently and receive a medium confidence level.

620 The Lake Cucao record potentially matches with 10 regionally known paleotsunami  
621 and paleoseismic events (Fig. 8, Tab. 3). Additionally, deposit cC matches to some  
622 extent with deposit hE in Lake Huelde and event D in Maullín, but weaker age control

623 in the Lake Cucao record for the last ~2000 yrs may inhibit a conclusive correlation.  
 624 The confidence level for both event deposit hE and cC are high, which supports the  
 625 hypothesis of same origin, because in no other instance is there a high confidence  
 626 tsunami deposit in Lake Huelde without a matching tsunami deposit in Lake Cucao  
 627 and vice versa. The only exception is the cryptic CE 1837 tsunami deposit, that was  
 628 recognised in Lake Huelde by IRSL dating (Kempf et al., 2015).

629 *Table 3: Regional age-correlation of paleotsunami and paleoseismic events.*

historical record	Cucao	Huelde	Mauullín	Rinihue Calafquen Villarrica
year of event	name in record (confidence level)	name in record (confidence level)	name in record	correlating event
1960	<b>cA (high)</b>	<b>hA (high)</b>	<b>A</b>	<b>yes</b>
1837	-	hB (high)	-	yes
1737	-	-	-	yes
1575	<b>cB (high)</b>	<b>hC (medium)</b>	<b>B</b>	<b>yes</b>
beyond record	-	hD (medium)	C	yes
	cC (high) (?)	hE (high)	D	yes
	<b>cD (medium)</b>	<b>hF (medium)</b>	<b>E</b>	<b>yes</b>
	cE (low) (?)	-	F	(?)
	<b>cF (high)</b>	<b>hG (high)</b>	<b>G</b>	<b>yes</b>
	<b>cG (medium)</b>	<b>hH (high)</b>	<b>H</b>	<b>yes</b>
	<b>cH (medium)</b>	<b>hI (medium)</b>	beyond record	<b>yes</b>
	cl (medium)	-		(?)
	<b>cJ (high)</b>	<b>hJ (high)</b>		<b>yes</b>
	<b>cK (high)</b>	<b>hK (high)</b>		<b>yes</b>
	cL (low)	-		no
	-	hL (low)		yes
	<b>cM (high)</b>	<b>hM (high)</b>		<b>yes</b>
	<b>cN (high)</b>	<b>hN (high)</b>		(?)
	cO (medium)	-		(?)
	beyond record	hO (medium)		(?)
		hP (medium)		(?)
		hQ (high)		beyond record

630

631 Deposit cE matches well with event F in Mauullín, however, Lake Huelde does not  
 632 record tsunami deposition in this period and in Mauullín the event was only recognised  
 633 by co-seismic subsidence and not with a tsunami deposit (Tab. 3) (Cisternas et al.,  
 634 2005; Kempf et al., 2017). Either Lake Cucao was relatively sensitive to tsunami  
 635 inundation at the time and recorded a minor tsunami that had no sedimentary impact  
 636 in Mauullín, Lake Huelde and other regional paleotsunami records. Or as the low  
 637 confidence level denotes, deposit cE is potentially not a tsunami deposit.

638 Both deposits cL and hL have only a minor sedimentary imprint in Lake Cucao and  
 639 Lake Huelde, respectively, with low confidence level on the interpretation as tsunami  
 640 deposits (cf. Kempf et al., 2017). If either deposit is a tsunami deposit, then the origin

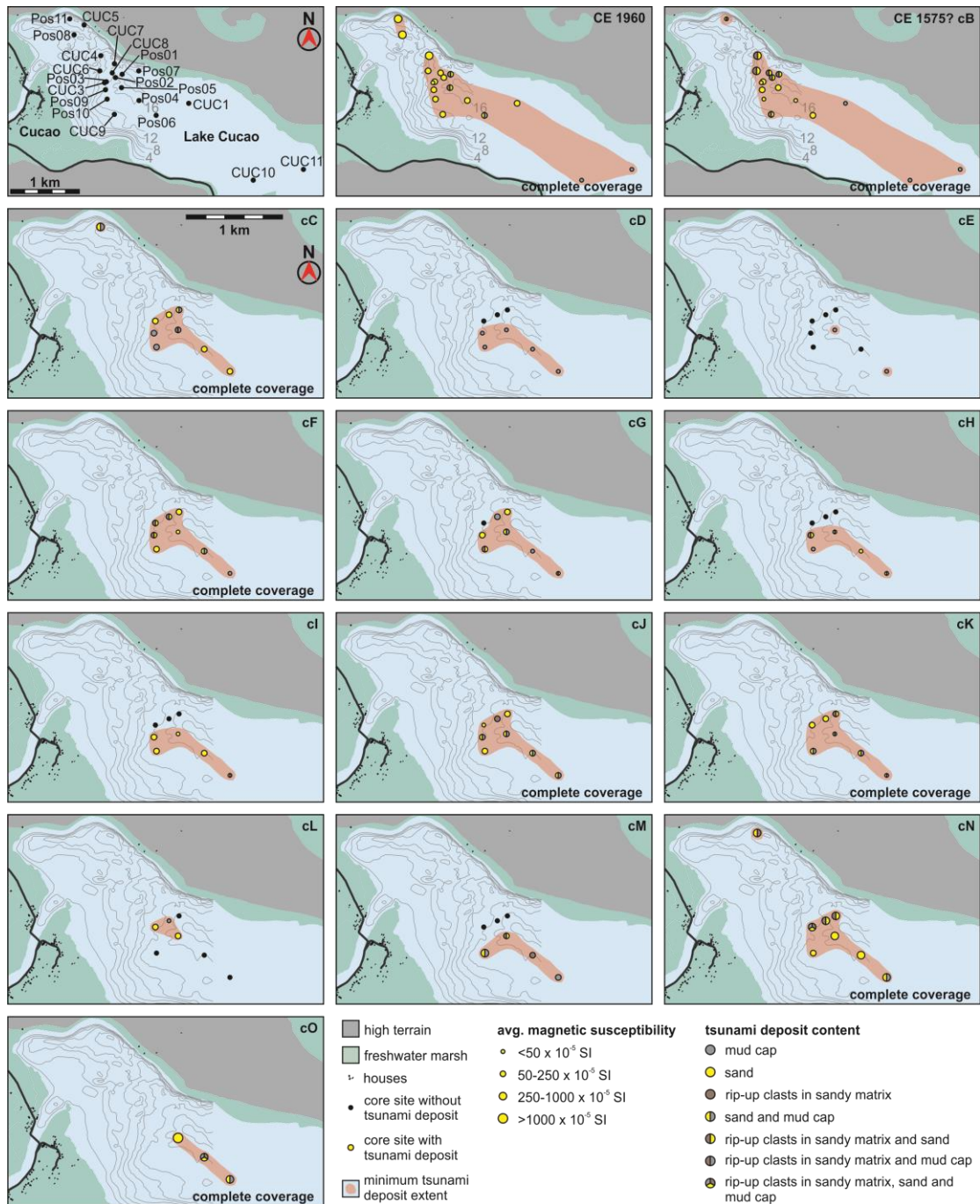
641 is probably a minor tsunami. The age-depth modelling in both records does not match  
642 the two deposits, so that it can be concluded that they are most likely not from the  
643 same event.

644 In contrast, for example, deposits cK and hK from Lake Cucao and Lake Huelde,  
645 respectively, share a similar clear (high confidence level), but not extreme  
646 sedimentary imprint in their respective records. The age-depth models match the two  
647 deposits, so it is likely that cK and hK were deposited during the same tsunami  
648 inundation event.

### 649 *5.5 Spatial perspective on tsunami deposits in a lake basin*

650 Event maps (Figs. 9 and 10) that summarise the sedimentary characteristics of the  
651 tsunami deposits visualise spatial trends of the tsunami deposits. The following  
652 conclusions are supported by the spatial data.

- 653 i) Mud rip-up clasts are limited to the proximal part of the lake basin (Fig.  
654 9). The tsunami deposit cO at core site Pos04 is the only exception. This  
655 trend seems plausible as it requires high energy water flow to erode and  
656 transport mud rip-up clasts. Dissipating energy in the fluid flow over  
657 distance would dictate that mud rip-up clasts would be the first particles to  
658 resist transport or remobilisation.
- 659 ii) For a large extent in the lake basin, tsunami deposits do not decrease in  
660 thickness. This contradicts the spatial trend in onshore tsunami deposits,  
661 where tsunami deposit thickness is influenced by the onshore morphology  
662 and tends to decrease with increasing run-up distance (Goto et al., 2014).  
663 This study has thickness data along up to ~3 km of inundation distance.  
664 Even for the tsunami deposit thickness data from CE 1960 and CE 1575  
665 (cB) with a ~3 km long transect no decreasing trend in thickness can be  
666 recognised. Logically, in the most distal parts of the record the tsunami  
667 deposit must wedge out, however, the core sites are not located in the area  
668 where this occurs.
- 669 iii) From the location where a tsunami deposit has a muddy component, the  
670 muddy characteristic in the tsunami deposits is always present in more  
671 distal locations. Examples are the tsunami deposits cF, cK or cM. This  
672 highlights one aspect of the reliability of coastal lakes to record tsunami  
673 deposits.
- 674 iv) To record tsunami deposition over large parts of a lacustrine basin, muddy  
675 grainsizes can be sufficient, e.g. tsunami deposit cD (Fig. 9). However,  
676 detection of those deposits is more difficult, because of the similarities to  
677 the surrounding regular lacustrine sediment. In the case of the muddy  
678 tsunami deposits in Lake Cucao the magnetic susceptibility was enough to  
679 indicate candidate clastic layers. In environments, where magnetic  
680 susceptibility cannot be used, other methods need to be tested, e.g. XRF  
681 scanning or a bio-marker analysis.



682

683 Figure 9: Event map of all tsunami deposit cA, i.e. CE 1960, to cO. The dots refer to  
 684 core sites that contain the stratigraphic interval in which the tsunami deposit is  
 685 located. Black dots mean the tsunami deposit was not detected. The size of the dot  
 686 is a function of the average magnetic susceptibility over the entire tsunami  
 687 deposit. The colour of the dot is a function of the sedimentary content of the  
 688 tsunami deposit. The red polygon depicts the lateral extent of the tsunami deposit.

689

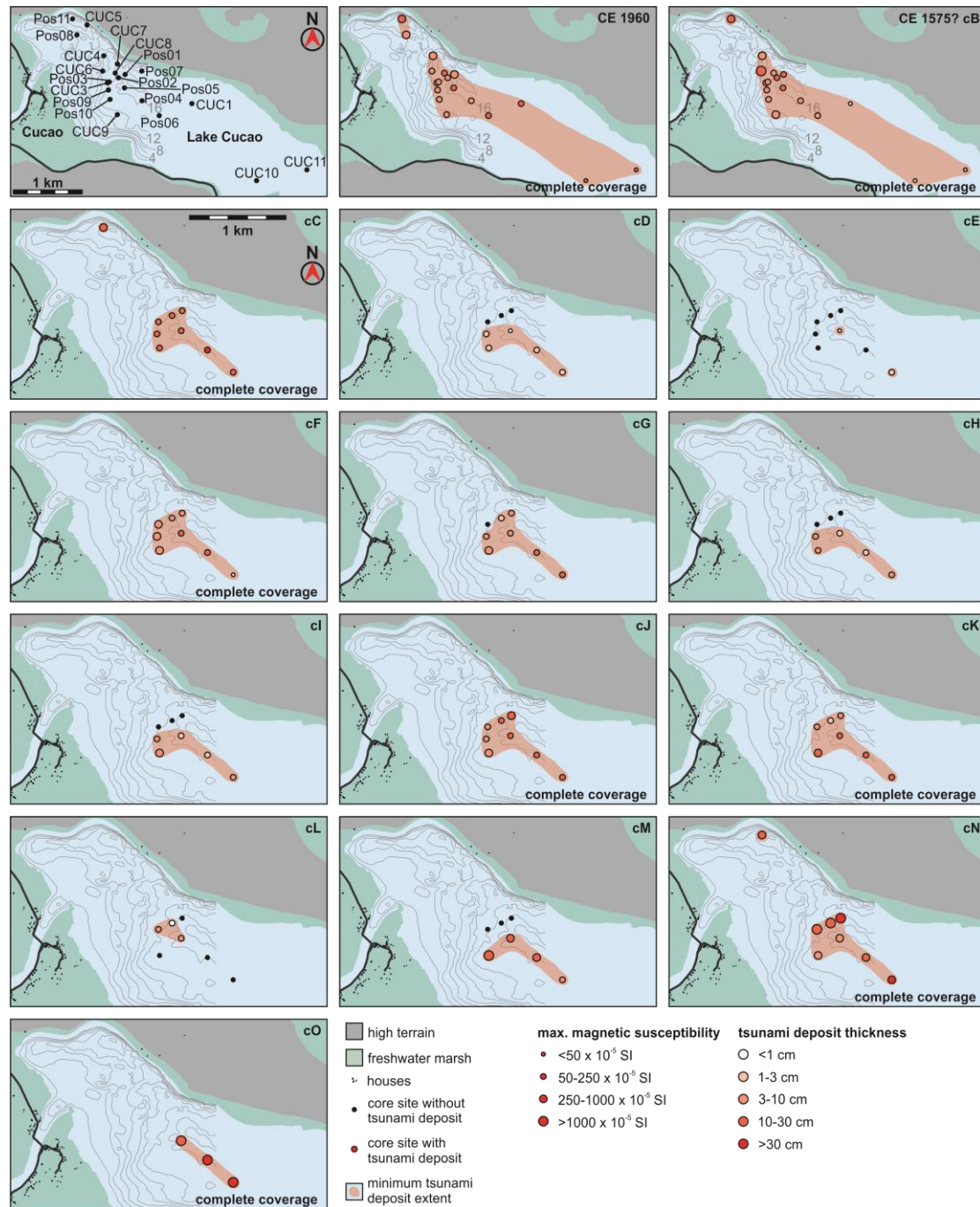


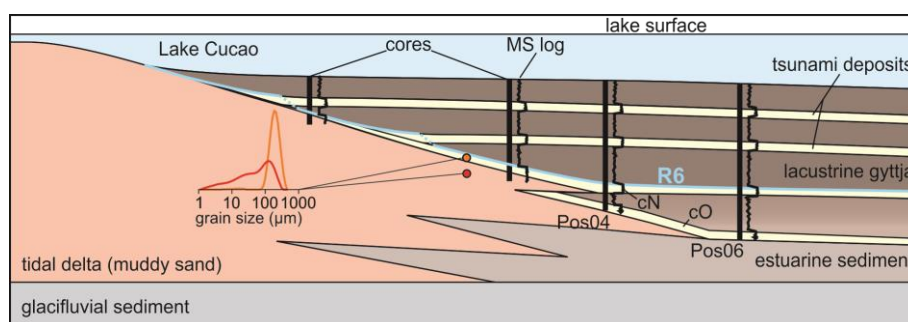
Figure 10: Event map of all tsunami deposit cA, i.e. CE 1960, to cO. The dots refer to core sites that contain the stratigraphic interval in which the tsunami deposit is located. Black dots mean the tsunami deposit was not detected. The size of the dot is a function of the maximum magnetic susceptibility of the tsunami deposit. The colour of the dot is a function of the tsunami deposit thickness in the core (darker red means thicker tsunami deposit). The red polygon depicts the lateral extent of the tsunami deposit.



699 **5.6 A conceptual model towards the origin and evolution of the lake basin**

700 In order to contrive a conceptual stratigraphic model of Lake Cucao that incorporates  
701 all sedimentologic evidence available, we begin with the topographical depression  
702 that is now occupied by Lake Cucao. The depression was a glacifluvial river valley  
703 (Glasser et al., 2008), which was submerged during the last global post-glacial  
704 eustatic sea-level rise (Siddall et al., 2003). During this transgression, the glacifluvial  
705 valley must have become an estuary, a similar evolution to lakes Lanalhue and Lleu  
706 Lleu ~500 km further north (Fig. 1) (Stefer et al., 2010). The oldest recovered  
707 sediment in core Pos04 (around tsunami deposit cN, reflector R6) is lacustrine,  
708 indicating that the barrier, which makes Lake Cucao a coastal lake, rather than an  
709 estuary, has been in place earlier than 4300 yrs ago.

710 Most likely aeolian sediments silled off the estuary and created the barrier and  
711 therewith the enclosed lake basin. The timing of the sill formation is unclear,  
712 however, one plausible hypothesis is that the expanding westerlies between 8.5 and  
713 5.5 ka (Lamy et al., 2010) may have enabled aeolian processes to create the sill.  
714 Aeolian processes are still prevailing in the coastal area west of Lake Cucao  
715 evidenced by an active dune belt.



716

717 *Figure 11: Conceptual stratigraphic model of Lake Cucao's sedimentary infill that*  
718 *summarizes the sedimentologic evidence available in the literature and in the*  
719 *results of this study. This model also explains the corrected age of tsunami*  
720 *deposit cO.*

721 Currently, Lake Cucao lies in the intertidal zone (Kempf et al., 2015; Villalobos et al.,  
722 2003), with saline water flowing into the lake from the Pacific during high tide. This  
723 process has been active at least sporadically since 4300 cal. yrs BP, evidenced by the  
724 convergent internal reflectors in the entire sediment sequence of U2 near the tidal  
725 channel. The same process has built up a tidal delta in Lake Cucao around the outlet.  
726 The conceptual stratigraphic model includes foresets of the tidal delta interfingering  
727 with lake basin and estuarine sediments (Fig. 11). One of these foresets may explain  
728 the muddy sand with the same characteristics as the exposed tidal delta sediments at  
729 the base of cores Pos02, Pos03 and Pos11. Clastic layer cN, interpreted as a tsunami  
730 deposit, is in direct contact to the muddy sand in all cores of the western part of the  
731 basin, except at Pos06. It appears that the formation of cN disrupted the deposition of  
732 muddy sand at the mentioned core locations. Clastic layer cN is thicker and coarser  
733 than all other clastic layers in most core locations. Additionally, the deposit correlates

734 chronologically to deposit hN, which is among the thicker and coarser tsunami  
735 deposits from the nearby Lake Huelde paleotsunami record (Kempf et al., 2017).

736 The overall extreme character relative to other tsunami deposits in the respective  
737 records of cN and hN may point towards an unusually strong tsunami. The end of  
738 foreset sedimentation after deposition of cN could be due to a large amount of either  
739 co-seismic uplift or subsidence during this event.

740 In the uplift scenario the lake system may stop interacting with the Pacific Ocean  
741 altogether. Tidal inflows into the lake would not occur and the processes, which form  
742 topsets and foresets on the tidal delta, would stop. Large amounts of co-seismic uplift  
743 can occur on the Chilean coast, e.g. in CE 1960 on Isla Guafo (Sievers et al., 1963).  
744 However, the geometry of the crust on and off Chiloé Island probably needs splay  
745 fault slip to generate such an uplift and an outstanding tsunami, as neither CE 1960,  
746 1837 nor 1575 created large co-seismic uplift there (Cisternas et al., 2017; Garrett et  
747 al., 2015; Plafker and Savage, 1970; Sievers et al., 1963).

748 The subsidence scenario seems more plausible, because of the example given by co-  
749 seismic subsidence around Cucao (~1 m) during the CE 1960 earthquake (Plafker and  
750 Savage, 1970). The subsidence would create accommodation, which would favour  
751 aggradation at the cost of progradation of the delta. During aggradation on the delta,  
752 the lake basin would accumulate organic-rich mud. Once aggradation used up the  
753 newly available accommodation, the lake system would switch back to progradation  
754 and begin forming the next interfingering foreset. In both examples, the presence of  
755 the tidal delta would be less dominant in the basinal sediments.

## 756 **6 Conclusions**

757 Based on sub-bottom profiles and numerous sediment cores, we add a new, long and  
758 continuous paleotsunami record in the rupture zone of the CE 1960 Great Chile  
759 Earthquake. We present following conclusions:

- 760 i) Sub-bottom profiles are crucial to understand the dynamic sedimentary system  
761 of coastal lakes and to help in selecting the most appropriate coring locations  
762 for paleotsunami research. Moreover, sub-bottom profiles may reveal  
763 sedimentary structures which can allow quantification of flow speed and  
764 depth, e.g. antidunes (Fig. 2).
- 765 ii) Dynamic coastal lakes with daily tidal inflow can be used for extracting long  
766 paleotsunami records. For the last 4300 yrs, Lake Cucao presents 15 tsunami  
767 deposits of mostly moderate to high confidence on the interpretation. This  
768 confidence level was based on physical sedimentary characteristics and  
769 contextual characteristics (Tab. 2), such as maximum magnetic susceptibility,  
770 traceability (Figs. 9 and 10), correlation to acoustic reflectors on the sub-  
771 bottom profiles (Fig. 6), the presence or lack of mud rip-up clasts (Figs. 5 and  
772 9), and age correlation with regional paleotsunami (Fig. 8). At least 10  
773 tsunami deposits correlate to paleotsunami deposits found in nearby Lake  
774 Huelde.

- 775       iii) The most complete tsunami record was found in core Pos05, 1.3 km from the  
776       lake outlet (tidal inlet) and a total 2.6 km from the present-day coastline. This  
777       relatively far inland location for regular tsunami deposition is facilitated by the  
778       river channel. There is evidence for tidal currents throughout the entire record,  
779       and thus persistent river connection, which allowed for continuous recording  
780       of tsunamis, despite co-, post- and inter-seismic relative sea level change in  
781       the late Holocene. However, such tidal currents can affect sediment dynamics,  
782       leading to variable depositional rates in space and time, adding complexity for  
783       reliable mapping and dating of tsunami deposits.
- 784       iv) This study underlines the many challenges and extraordinary advantages  
785       associated to paleotsunami research on coastal lakes and demonstrates how  
786       indispensable geophysical mapping and numerous coring sites are in  
787       understanding the depositional environment of dynamic coastal lakes for  
788       extracting high-quality, long and continuous paleotsunami records.

### 789       **Acknowledgments**

790       PK acknowledges financial support by the Special Research Fund of Ghent University  
791       (BOF), JM from the Chilean Fondecyt projects nr. 1150346 and 1150321, MVD from  
792       the Research Foundation Flanders (FWO travel grant K201512N), RU from  
793       CONICYT/FONDAP/15130015. We thank Koen De Rycker, Willem Vandoorne and  
794       Gauvain Wiemer for fieldwork support, Dr. Claire Schepens and Dr. Eric Achten for  
795       CT-scanner support. IHS Markit is acknowledged for providing the Kingdom seismic  
796       interpretation software within their educational grant program.

### 797       **References**

- 798       Allen, J.R.L., 1984. *Sedimentary Structures: Their Character and Physical Basis*.  
799       Elsevier, Amsterdam.
- 800       Amante, C., Eakins, B.W., 2009. ETOPO1 1 Arc-Minute Global Relief Model:  
801       Procedures, Data Sources and Analysis. NOAA Technical Memorandum  
802       NESDIS NGDC-24. National Geophysical Data Center, NOAA.  
803       doi:10.7289/V5C8276M
- 804       Atwater, B.F., Cisternas, M., Yulianto, E., Prendergast, A.L., Jankaew, K., Eipert,  
805       A.A., Ignatius, W., Fernando, S., Tejakusuma, I., 2013. The 1960 tsunami on  
806       beach-ridge plains near Maullín, Chile: Landward descent, renewed breaches,  
807       aggraded fans, multiple predecessors. *Andean Geology* 40, 393–418.  
808       doi:10.5027/andgeoV40n3-a01
- 809       Blaauw, M., Christen, J.A., 2011. Flexible Paleoclimate Age-Depth Models Using an  
810       Autoregressive Gamma Process. *Bayesian Analysis* 6, 457–474. doi:10.1214/11-  
811       BA618
- 812       Carling, P., Burr, D., Brennand, T.A., 2009. A review of open-channel megaflood  
813       depositional landforms on Earth and Mars A review of open-channel megaflood  
814       depositional landforms on Earth and Mars, in: Burr, D.M., Carling, P.A., Baker,

- 815 V.R. (Eds.), *Megaflooding on Earth and Mars*. pp. 33–49.  
816 doi:10.1017/CBO9780511635632.003
- 817 Chagué-Goff, C., Schneider, J.-L., Goff, J.R., Dominey-Howes, D., Strotz, L., 2011.  
818 Expanding the proxy toolkit to help identify past events — Lessons from the  
819 2004 Indian Ocean Tsunami and the 2009 South Pacific Tsunami. *Earth-Science*  
820 *Reviews* 107, 107–122. doi:10.1016/j.earscirev.2011.03.007
- 821 Chagué-Goff, C., Szczuciński, W., Shinozaki, T., 2017. Applications of geochemistry  
822 in tsunami research: A review. *Earth-Science Reviews* 165, 203–244.  
823 doi:https://doi.org/10.1016/j.earscirev.2016.12.003
- 824 Cisternas, M., Atwater, B.F., Torrejón, F., Sawai, Y., Machuca, G., Lagos, M., Eipert,  
825 A., Youlton, C., Salgado, I., Kamataki, T., Shishikura, M., Rajendran, C.P.,  
826 Malik, J.K., Rizal, Y., Husni, M., 2005. Predecessors of the giant 1960 Chile  
827 earthquake. *Nature* 437, 404–407. doi:10.1038/nature03943
- 828 Cisternas, M., Garrett, E., Wesson, R., Dura, T., Ely, L.L., 2017. Unusual geologic  
829 evidence of coeval seismic shaking and tsunamis shows variability in earthquake  
830 size and recurrence in the area of the giant 1960 Chile earthquake. *Marine*  
831 *Geology* 385, 101–113. doi:10.1016/j.margeo.2016.12.007
- 832 Dura, T., Cisternas, M., Horton, B.P., Ely, L.L., Nelson, A.R., Wesson, R.L.,  
833 Pilarczyk, J.E., 2015. Coastal evidence for Holocene subduction-zone  
834 earthquakes and tsunamis in central Chile. *Quaternary Science Reviews* 113, 93–  
835 111. doi:10.1016/j.quascirev.2014.10.015
- 836 Dura, T., Engelhart, S.E., Vacchi, M., Horton, B.P., Kopp, R.E., Peltier, W.R.,  
837 Bradley, S., 2016. The Role of Holocene Relative Sea-Level Change in  
838 Preserving Records of Subduction Zone Earthquakes. *Current Climate Change*  
839 *Reports* 2, 86–100. doi:10.1007/s40641-016-0041-y
- 840 Ely, L.L., Cisternas, M., Wesson, R.L., Dura, T., 2014. Five centuries of tsunamis and  
841 land-level changes in the overlapping rupture area of the 1960 and 2010 Chilean  
842 earthquakes. *Geology* 42, 995–998. doi:10.1130/G35830.1
- 843 Fedorov, A. V, Brierley, C.M., Emanuel, K., 2010. Tropical cyclones and permanent  
844 El Niño in the early Pliocene epoch. *Nature* 463, 1066–1070.  
845 doi:10.1038/nature08831
- 846 Fritz, H.M., Phillips, D.A., Okayasu, A., Shimozono, T., Liu, H., Mohammed, F.,  
847 Skanavis, V., Synolakis, C.E., Takahashi, T., 2012. The 2011 Japan tsunami  
848 current velocity measurements from survivor videos at Kesenuma Bay using  
849 LiDAR. *Geophysical Research Letters* 39, 6. doi:10.1029/2011GL050686
- 850 Garrett, E., Shennan, I., Woodroffe, S.A.A., Cisternas, M., Hocking, E.P.P., Gulliver,  
851 P., 2015. Reconstructing paleoseismic deformation, 2: 1000 years of great  
852 earthquakes at Chucalén, south central Chile. *Quaternary Science Reviews* 113,  
853 112–122. doi:10.1016/j.quascirev.2014.10.010

- 854 Glasser, N.F., Jansson, K.N., Harrison, S., Kleman, J., 2008. The glacial  
855 geomorphology and Pleistocene history of South America between 38°S and  
856 56°S. *Quaternary Science Reviews* 27, 365–390.  
857 doi:10.1016/j.quascirev.2007.11.011
- 858 Goto, K., Hashimoto, K., Sugawara, D., Yanagisawa, H., Abe, T., 2014. Spatial  
859 thickness variability of the 2011 Tohoku-oki tsunami deposits along the coastline  
860 of Sendai Bay. *Marine Geology* 358, 38–48. doi:10.1016/j.margeo.2013.12.015
- 861 Heiri, O., Lotter, A.F., Lemcke, G., 2001. Loss on ignition as a method for estimating  
862 organic and carbonate content in sediments : reproducibility and comparability of  
863 results. *Journal of Paleolimnology* 25, 101–110. doi:10.1023/A:1008119611481
- 864 Hogg, A.G., Hua, Q., Blackwell, P.G., Niu, M., Buck, C.E., Guilderson, T.P., Heaton,  
865 T.J., Palmer, J.G., Reimer, P.J., Reimer, R.W., Turney, C.S.M., Zimmerman,  
866 S.R.H., 2013. SHCal13 Southern Hemisphere Calibration, 0–50,000 Years cal  
867 BP. *Radiocarbon* 55, 1889–1903. doi:10.2458/azu\_js\_rc.55.16783
- 868 Kelsey, H.M., Engelhart, S.E., Pilarczyk, J.E., Horton, B.P., Rubin, C.M., Daryono,  
869 M.R., Ismail, N., Hawkes, A.D., Bernhardt, C.E., Cahill, N., 2015.  
870 Accommodation space, relative sea level, and the archiving of paleo-earthquakes  
871 along subduction zones. *Geology* 43, 675–678. doi:10.1130/G36706.1
- 872 Kelsey, H.M., Nelson, A.R., Hemphill-Haley, E., Witter, R.C., 2005. Tsunami history  
873 of an Oregon coastal lake reveals a 4600 yr record of great earthquakes on the  
874 Cascadia subduction zone. *Geological Society of America Bulletin* 117, 1009–  
875 1032. doi:10.1130/B25452.1
- 876 Kempf, P., 2016. Tsunamis in south central Chile: evidence from coastal lakes. Ghent  
877 University.
- 878 Kempf, P., Moernaut, J., Batist, M. De, 2018. Bimodal Recurrence Pattern of  
879 Tsunamis in South-Central Chile: A Statistical Exploration of Paleotsunami  
880 Data. *Seismological Research Letters* 90, 194–202. doi:10.1785/0220180204
- 881 Kempf, P., Moernaut, J., Van Daele, M., Vandoorne, W., Pino, M., Urrutia, R., De  
882 Batist, M., 2017. Coastal lake sediments reveal 5500 years of tsunami history in  
883 south central Chile. *Quaternary Science Reviews* 161, 99–116.  
884 doi:http://doi.org/10.1016/j.quascirev.2017.02.018
- 885 Kempf, P., Moernaut, J., Van Daele, M., Vermassen, F., Vandoorne, W., Pino, M.,  
886 Urrutia, R., Schmidt, S., Garrett, E., De Batist, M., 2015. The sedimentary record  
887 of the 1960 tsunami in two coastal lakes on Isla de Chiloé, south central Chile.  
888 *Sedimentary Geology* 328, 73–86. doi:10.1016/j.sedgeo.2015.08.004
- 889 Kennedy, J., 1963. The mechanics of dunes and antidunes in erodible-bed channels.  
890 *Journal of Fluid Mechanics* 16, 521–544. doi:10.1017/S0022112063000975
- 891 Kortekaas, S., Dawson, A.G., 2007. Distinguishing tsunami and storm deposits: An  
892 example from Martinhal, SW Portugal. *Sedimentary Geology* 200, 208–221.

- 893        doi:<https://doi.org/10.1016/j.sedgeo.2007.01.004>
- 894    Lamy, F., Kilian, R., Arz, H.W., Francois, J.-P., Kaiser, J., Prange, M., Steinke, T.,  
895        2010. Holocene changes in the position and intensity of the southern westerly  
896        wind belt. *Nature Geosci* 3, 695–699.
- 897    Lee, Sang Hoon, Jung, W.-Y., Bahk, J.J., Gardner, J.M., Kim, J.K., Lee, Su Hwan,  
898        2013. Depositional features of co-genetic turbidite–debrite beds and possible  
899        mechanisms for their formation in distal lobated bodies beyond the base-of-  
900        slope, Ulleung Basin, East Sea (Japan Sea). *Marine Geology* 346, 124–140.  
901        doi:10.1016/j.margeo.2013.09.001
- 902    Lomnitz, C., 2004. Major Earthquakes of Chile: A Historical Survey, 1535-1960.  
903        *Seismological Research Letters* 75, 368–378. doi:10.1785/gssrl.75.3.368
- 904    Lomnitz, C., 1970. Major Earthquakes and Tsunamis in Chile during the period 1535  
905        to 1955. *Geologische Rundschau* 59, 938–960.
- 906    Moernaut, J., Van Daele, M., Fontijn, K., Heirman, K., Kempf, P., Pino, M.,  
907        Valdebenito, G., Urrutia, R., Strasser, M., De Batist, M., 2018. Larger  
908        earthquakes recur more periodically: New insights in the megathrust earthquake  
909        cycle from lacustrine turbidite records in south-central Chile. *Earth and Planetary*  
910        *Science Letters* 481, 9–19. doi:<https://doi.org/10.1016/j.epsl.2017.10.016>
- 911    Moernaut, J., Van Daele, M., Heirman, K., Fontijn, K., Strasser, M., Pino, M.,  
912        Urrutia, R., De Batist, M., 2014. Lacustrine turbidites as a tool for quantitative  
913        earthquake reconstruction: New evidence for a variable rupture mode in south  
914        central Chile. *Journal of Geophysical Research: Solid Earth* 119, 1607–1633.  
915        doi:10.1002/2013JB010738
- 916    Moreno, M.S., Bolte, J., Klotz, J., Melnick, D., 2009. Impact of megathrust geometry  
917        on inversion of coseismic slip from geodetic data: Application to the 1960 Chile  
918        earthquake. *Geophysical Research Letters* 36, L16310.  
919        doi:10.1029/2009GL039276
- 920    Nentwig, V., Bahlburg, H., Górecka, E., Huber, B., Bellanova, P., Witkowski, A.,  
921        Encinas, A., 2018. Multiproxy analysis of tsunami deposits—The Tirúa example,  
922        central Chile. *Geosphere* 14, 1067–1086. doi:10.1130/GES01528.1
- 923    Nentwig, V., Tsukamoto, S., Frechen, M., Bahlburg, H., 2015. Reconstructing the  
924        tsunami record in Tirúa, Central Chile beyond the historical record with quartz-  
925        based SAR-OSL. *Quaternary Geochronology* 30, 299–305.  
926        doi:<http://dx.doi.org/10.1016/j.quageo.2015.05.020>
- 927    Peters, R., Jaffe, B., Gelfenbaum, G., 2007. Distribution and sedimentary  
928        characteristics of tsunami deposits along the Cascadia margin of western North  
929        America. *Sedimentary Geology* 200, 372–386. doi:10.1016/j.sedgeo.2007.01.015
- 930    Phantuwongraj, S., Choowong, M., Nanayama, F., Hisada, K.-I., Charusiri, P.,  
931        Chutakositkanon, V., Pailoplee, S., Chabangbon, A., 2013. Coastal geomorphic

- 932 conditions and styles of storm surge washover deposits from Southern Thailand.  
933 *Geomorphology* 192, 43–58. doi:10.1016/j.geomorph.2013.03.016
- 934 Plafker, G., Savage, J.C., 1970. Mechanism of the Chilean Earthquakes of May 21  
935 and 22 , 1960. *Geological Society of America Bulletin* 81, 1001–1030.  
936 doi:10.1130/0016-7606(1970)81
- 937 Reinhardt, E.G., Nairn, R.B., Lopez, G., 2010. Recovery estimates for the Río Cruces  
938 after the May 1960 Chilean earthquake. *Marine Geology* 269, 18–33.  
939 doi:10.1016/j.margeo.2009.12.003
- 940 Siddall, M., Rohling, E.J., Almogi-Labin, A., Hemleben, C., Meischner, D.,  
941 Schmelzer, I., Smeed, D.A., 2003. Sea-level fluctuations during the last glacial  
942 cycle. *Nature* 423, 853–858.
- 943 Sievers, H., Villegas, G.C., Barros, G., 1963. The seismic sea wave of 22 May 1960  
944 along the Chilean coast. *Bulletin of the Seismological Society of America* 53,  
945 1125–1190.
- 946 Stefer, S., Moernaut, J., Melnick, D., Echtler, H.P., Arz, H.W., Lamy, F., De Batist,  
947 M., Oncken, O., Haug, G.H., 2010. Forearc uplift rates deduced from sediment  
948 cores of two coastal lakes in south-central Chile. *Tectonophysics* 495, 129–143.  
949 doi:http://dx.doi.org/10.1016/j.tecto.2009.05.006
- 950 Valdovinos, C., Pedreros, P., 2007. Geographic variations in shell growth rates of the  
951 mussel *Diplodon chilensis* from temperate lakes of Chile: Implications for  
952 biodiversity conservation. *Limnologica* 37, 63–75.  
953 doi:https://doi.org/10.1016/j.limno.2006.08.007
- 954 Van Daele, M., Araya-Cornejo, C., Pille, T., Vanneste, K., Moernaut, J., Schmidt, S.,  
955 Kempf, P., Meyer, I., Cisternas, M., 2019. Distinguishing intraplate from  
956 megathrust earthquakes using lacustrine turbidites. *Geology* 47, 127–130.
- 957 Van Daele, M., Cnudde, V., Duyck, P., Pino, M., Urrutia, R., De Batist, M., 2014.  
958 Multidirectional, synchronously-triggered seismo-turbidites and debrites  
959 revealed by X-ray computed tomography (CT). *Sedimentology* 61, 861–880.  
960 doi:10.1111/sed.12070
- 961 Villalobos, L., Parra, O., Grandjean, M., Jaque, E., Woelfl, S., Campos, H., 2003. A  
962 study of the river basins and limnology of five humic lakes on Chiloé Island.  
963 *Revista chilena de historia natural* 76. doi:10.4067/S0716-078X2003000400003
- 964 Wesson, R.L., Melnick, D., Cisternas, M., Moreno, M., Ely, L.L., 2015. Vertical  
965 deformation through a complete seismic cycle at Isla Santa Maria, Chile. *Nature*  
966 *Geoscience* 8, 547–551.
- 967